

Feedback-regulated star formation and escape of LyC photons from mini-haloes during reionisation

Taysun Kimm^{1*}, Harley Katz¹, Martin Haehnelt¹, Joakim Rosdahl², Julien Devriendt^{3,4},
Adrianne Slyz³

¹ Kavli Institute for Cosmology and Institute of Astronomy, Madingley Road, Cambridge CB3 0HA, UK

² Leiden Observatory, Leiden University, P.O. Box 9513, 2300 RA, Leiden, The Netherlands

³ Astrophysics, University of Oxford, Denys Wilkinson Building, Keble Road, Oxford OX1 3RH, UK

⁴ Observatoire de Lyon, UMR 5574, 9 avenue Charles Andre, F-69561 Saint Genis Laval, France

5 March 2024

ABSTRACT

Reionisation in the early Universe is likely driven by dwarf galaxies. Using cosmological radiation-hydrodynamic simulations, we study star formation and the escape of Lyman continuum (LyC) photons from mini-haloes with $M_{\text{halo}} \lesssim 10^8 M_{\odot}$. Our simulations include a new thermo-turbulent star formation model, non-equilibrium chemistry, and relevant stellar feedback processes (photoionisation by young massive stars, radiation pressure, and mechanical supernova explosions). We find that feedback reduces star formation very efficiently in mini-haloes, resulting in the stellar mass consistent with the slope and normalisation reported in Kimm & Cen (2014) and the empirical stellar mass-to-halo mass relation derived in the local Universe. Because star formation is stochastic and dominated by a few gas clumps, the escape fraction in mini-haloes is generally determined by radiation feedback (heating due to photoionisation), rather than supernova explosions. We also find that the photon number-weighted mean escape fraction in mini-haloes is higher ($\sim 20\text{--}40\%$) than that in atomic-cooling haloes, although the instantaneous fraction in individual haloes varies significantly. The escape fraction from Pop III stars is found to be significant ($\gtrsim 10\%$) only when the mass is greater than $\sim 100 M_{\odot}$. Based on simple analytic calculations, we show that LyC photons from mini-haloes are, despite their high escape fractions, of minor importance for reionisation due to inefficient star formation. We confirm previous claims that stars in atomic-cooling haloes with masses $10^8 M_{\odot} \lesssim M_{\text{halo}} \lesssim 10^{11} M_{\odot}$ are likely to be the most important source of reionisation.

Key words: Cosmology: dark ages, reionization, first stars – Cosmology: early Universe – galaxies: high-redshift

1 INTRODUCTION

Observations of Lyman α opacities in the spectra of quasi-stellar objects (QSOs) at high redshift have shown unambiguously that the Universe becomes nearly transparent to LyC photons ($\lambda \leq 912 \text{ \AA}$) at $z \sim 6$ (Fan et al. 2001; Becker et al. 2001; Fan et al. 2006; McGreer et al. 2015). Several candidates are identified as a potential source of reionisation, including dwarf galaxies (e.g., Couchman & Rees 1986; Madau et al. 1999), active galactic nuclei (e.g., Shapiro & Giroux 1987; Haiman & Loeb 1998), accretion shock (Dopita et al. 2011), globular clusters (Ricotti 2002; Katz & Ricotti 2013, 2014), and X-rays from accreting stellar-mass black holes (e.g., Madau et al. 2004; Ricotti & Ostriker 2004; Mirabel et al. 2011). Many studies agree that the primary source of reionisation is likely to be massive stars in dwarf galaxies (Haehnelt et al. 2001;

Cowie et al. 2009; Fontanot et al. 2014; Madau & Fragos 2016, c.f., Madau & Haardt 2015); however, the timescale over which reionisation occurred and the mass range of haloes which provided the majority of the ionising photons are issues that remain unresolved (e.g., Bolton & Haehnelt 2007; Kuhlen & Faucher-Giguère 2012; Ahn et al. 2012; Wise et al. 2014).

The two critical ingredients for reionisation are star formation and escaping LyC photons. The former describes how many LyC photons are available from massive stars, while the latter determines what fraction are actually used to ionise the intergalactic medium (IGM). Unsurprisingly, the prediction of both quantities is very challenging, as galaxy evolution involves highly non-linear processes, such as the interaction between the ISM and feedback from stars. For this reason, numerical studies often report discrepant results on the escape fraction. An early attempt by Gnedin et al. (2008) suggested that the escape fraction roughly increases with halo mass in the range $10^{10}\text{--}10^{12} M_{\odot}$, because stellar disks

* e-mail: tkimm@ast.cam.ac.uk

in lower mass haloes tend to be embedded in gaseous disks in their simulations. Wise & Cen (2009) also found a positive correlation between the escape fraction and halo mass in the range $10^6 - 10^{10} M_\odot$, but as Wise et al. (2014) pointed out, this may have been caused by the initial strong starburst due to the absence of cooling while constructing the initial conditions of the simulations. On the contrary, by post-processing hydrodynamics simulations with strong stellar feedback, Razoumov & Sommer-Larsen (2010) concluded that low-mass haloes ($\sim 10^8 M_\odot$) show a higher escape fraction of $\sim 100\%$, while less than 10% of LyC photons escape from the massive haloes with mass $10^{11} M_\odot$. A negative dependence on halo mass in the atomic-cooling regime is also found in other large cosmological simulations based on post-processing (Yajima et al. 2011; Paardekooper et al. 2013). Large-scale simulations often predict very high escape fractions of $f_{\text{esc}} \gtrsim 50\%$ in atomic cooling haloes, but these conclusions may be subject to numerical resolution (Ma et al. 2015; Paardekooper et al. 2015) and how the escape fraction is measured (i.e. whether or not it is photon number-weighted (Kimm & Cen 2014)). Paardekooper et al. (2015) pointed out that significant absorption of LyC photons occurs on giant molecular cloud scales (i.e. 10 pc). Recent theoretical work based on effective feedback with high numerical resolution ($\lesssim 10$ pc) suggests that, on average, only $\sim 10\%$ of LyC photons escape from their host haloes with the mass range $10^8 M_\odot \lesssim M_{\text{halo}} \lesssim 10^{11} M_\odot$ (Kimm & Cen 2014; Ma et al. 2015; Xu et al. 2016). The only exception to this relatively low escape fraction found in numerical simulations is mini-haloes where 40–60% of the ionising photons escape the galaxies and contribute to the ionisation of the IGM (Wise et al. 2014; Xu et al. 2016).

In observations, the leakage of LyC photons is measured via the relative flux density ratio ($F_{\text{UV}}/F_{\text{LyC}}$) between the ionising part of the spectrum at 900 \AA and the non-ionising part at 1500 \AA (Steidel et al. 2001). Once absorption due to the IGM is corrected (e.g., Inoue et al. 2014), one can estimate the absolute escape fraction assuming a ratio of the intrinsic luminosity at 900 \AA and 1500 \AA appropriate for the observed multi-band photometric data. The detection of LyC photons in the local Universe is limited to starburst galaxies (Leitet et al. 2011, 2013; Borthakur et al. 2014; Leitherer et al. 2016), where generally small escape fractions ($\lesssim 5\%$) are observed. Star-forming galaxies at $z \sim 1$ with LyC detection also show low escape fractions of a few percent (Siana et al. 2007, 2010; Bridge et al. 2010; Rutkowski et al. 2016). Efficient LyC leakers ($f_{\text{esc}} \gtrsim 10\%$) seem to be more common at higher redshift ($z \gtrsim 3$, e.g., Reddy et al. 2016), but only a handful of cases are confirmed as robust detections which are not affected by contamination due to low-redshift interlopers along the line of sight (Mostardi et al. 2015; Shapley et al. 2016; Leethochawalit et al. 2016). The average, relative escape fraction in nearly all observations is found to be very small, even at high redshift ($f_{\text{esc}}^{\text{rel}} \lesssim 2\%$, Grazian et al. 2016; Vanzella et al. 2010; Boutsia et al. 2011; Siana et al. 2015; Mostardi et al. 2015), and appears to be in tension with the $f_{\text{esc}} \sim 10\%$ needed to reconcile the observed luminosity of high-redshift galaxies with observational constraints on the evolution of the average neutral hydrogen fraction. However, it should be noted that these estimates mostly focus on small galaxies of mass $M_{\text{star}} \leq 10^8 M_\odot$ or $M_{\text{UV}} \gtrsim -18$ at $z \geq 6$, whereas observed samples are biased towards bright galaxies ($M_{\text{UV}} \lesssim -20$, e.g., Grazian et al. 2016). Because star formation in small galaxies is more bursty than in bright galaxies observed at lower redshift (e.g., Speagle et al. 2014), it is conceivable that the star-forming clouds are disrupted more efficiently in simulated galaxies, resulting in

higher escape fractions (e.g., Kimm & Cen 2014; Cen & Kimm 2015). Moreover, since the simulated galaxies are more metal-poor than the observed bright galaxies, they are likely less affected by dust compared to observed galaxies (e.g., Izotov et al. 2016). Finally, as pointed out by Cen & Kimm (2015), individual measurements of the escape fraction may underestimate the three dimensional escape fraction, especially when the escape fraction is small.

Unlike the observed LyC flux that conveys information about the instantaneous escape fraction, the Thompson electron optical depth (τ_e) derived from the polarisation signal of cosmic microwave background (CMB) photons provides a useful measure of how extended reionisation was in the early Universe. The analysis of the nine-year Wilkinson Microwave Anisotropy Probe (WMAP9) observations suggested a high electron optical depth of $\tau_e = 0.089 \pm 0.014$ (Hinshaw et al. 2013), indicating that ionised hydrogen (HII) bubbles are likely to have grown relatively early. However, the observed number density of bright galaxies in the ultraviolet (UV) ($M_{\text{UV}} \lesssim -17$) is unable to explain such a high τ_e (e.g., Bunker et al. 2010; Finkelstein et al. 2010; Bouwens et al. 2012). By taking a parametric form of the UV luminosity density, motivated by observations of the Hubble Ultra Deep Field, Robertson et al. (2013) showed that the inclusion of small dwarf galaxies with $-17 \leq M_{\text{UV}} \leq -13$ can increase τ_e to a higher value of 0.07, provided that 20% of LyC photons escape from the dark matter haloes. Wise et al. (2014) claim that mini-haloes of mass $M_{\text{halo}} \leq 10^8 M_\odot$, corresponding to $M_{\text{UV}} \gtrsim -13$, may be able to provide a large number of LyC photons to the IGM as LyC photons escape freely from their host halo. Because the mini-haloes emerge first and they are abundant in the early Universe ($z \geq 15$), the authors find that the resulting $\tau_e \approx 0.09$ can easily accommodate the WMAP9 analysis, demonstrating the potential importance of mini-haloes to reionisation of the Universe (see also Ahn et al. 2012).

However, a more accurate modelling of dust emission in our Galaxy (Planck Collaboration et al. 2014) and the use of the low frequency instrument on the Planck satellite lead to a decrease in the optical depth to $\tau_e = 0.066 \pm 0.016$ (Planck Collaboration et al. 2015). The latest results utilising the high frequency instrument to measure the low-multipole polarisation signal point to a possibility of an even lower value of $\tau_e = 0.055 \pm 0.009$ (Planck Collaboration et al. 2016). Furthermore, recent findings of significant Ly α opacity fluctuations on large scales in absorption spectra of $5 \lesssim z \lesssim 6$ QSOs (Becker et al. 2015) and the observed rapid evolution of Ly α emitters at $z > 6$ (Ono et al. 2012; Caruana et al. 2014; Schenker et al. 2014; Pentericci et al. 2014; Tilvi et al. 2014; Matthee et al. 2015) suggest that reionisation may have ended later than previously thought (e.g., Chardin et al. 2015; Choudhury et al. 2015; Davies & Furlanetto 2016, c.f., Haardt & Madau 2012; Mesinger et al. 2015). If the contribution from mini-haloes were important for reionisation, this may potentially be in tension with the reduced τ_e measurement and the long Ly α troughs still observed at $z \sim 5.6$ (Becker et al. 2015). Therefore, in this study, we revisit the importance of mini-haloes and assess their role in reionisation using state-of-the-art numerical simulations.

This paper is organised as follows. In Section 2, we describe the physical ingredients used in our cosmological, radiation-hydrodynamic simulations. The measurements of the escape fraction and star formation in the simulations are presented in Section 3. Section 4 discusses the mechanisms responsible for the escape of LyC photons and whether or not the ionising radiation from mini-haloes is crucial to reionisation of the Universe. We summarise our findings in Section 5.

2 SIMULATION

We use RAMSES-RT, a radiation hydrodynamics code with adaptive mesh refinement, (Teyssier 2002; Rosdahl et al. 2013; Rosdahl & Teyssier 2015), to study reionisation due to starlight in mini-haloes with $10^6 \lesssim M_{\text{halo}}/M_{\odot} \lesssim 10^8$. The cosmological initial conditions are generated using MUSIC (Hahn & Abel 2011), with the cosmological parameters ($\Omega_m = 0.288$, $\Omega_{\Lambda} = 0.712$, $\Omega_b = 0.045$, $H_0 = 69.33 \text{ km s}^{-1} \text{ Mpc}^{-1}$, $n_s = 0.971$, and $\sigma_8 = 0.830$) consistent with the WMAP9 results (Hinshaw et al. 2013). We first run dark matter only simulations with volume $(2 \text{ Mpc}/h)^3$, and identify nine regions hosting a halo of mass $\approx 10^8 M_{\odot}$ at $7 \leq z \leq 11$. The initial conditions for the zoom-in regions are then generated with a higher dark matter resolution of $90 M_{\odot}$ to resolve each halo with more than 10,000 dark matter particles. We ensure that the haloes are not contaminated by coarse dark matter particles.

We solve the Euler equations using a HLLC scheme (Toro et al. 1994), with the typical courant number of 0.7. The Poisson equation is solved using a multigrid method (Guillet & Teyssier 2011). For the transport of multiple photon groups, RAMSES-RT uses a moment-based method with M1 closure for the Eddington tensor (Rosdahl et al. 2013; Rosdahl & Teyssier 2015, see also Aubert & Teyssier 2008). We adopt a GLF scheme to solve the advection of the photon fluids. Because the hydrodynamics is fully coupled to the radiation, the computational time step is usually determined by the speed of light. Since we are interested in the escaping flux, which is a conserved quantity, we use a reduced speed of light approximation ($\tilde{c} = 3 \times 10^{-3} c$) to keep the computational cost low, where c is the full speed of light.

Each zoom-in simulation is covered with 128^3 root cells, and we allow for further refinement of the computational grid to achieve a maximum physical resolution of 0.7 pc. To do so, we adopt two different refinement criteria. First, a cell is refined if the total baryonic plus dark matter inside each cell exceeds 8 times the mass of a dark matter particle (i.e. $720 M_{\odot}$). Second, we enforce that the thermal Jeans length is resolved by at least 32 cells until it reaches the maximum resolution. Although the use of the latter condition is computationally expensive, it makes our simulations more robust than previous simulations, as the turbulent properties of gas can be more accurately captured (Federrath et al. 2011; Turk et al. 2012; Meece et al. 2014).

We identify dark matter haloes with the AdaptaHop algorithm (Tweed et al. 2009; Aubert et al. 2004). The centre of a dark matter halo is chosen as the centre of mass of the star particles in the halo. If a halo is devoid of stars, we use the densest location of the halo. The virial mass and radius of a halo is computed such that the mean density within the virial sphere is equivalent to $\Delta_{\text{crit}} \rho_{\text{crit}}$, where ρ_{crit} is the critical density of the universe ($3H(z)^2/8\pi G$), $\Delta_{\text{crit}} = 18\pi^2 + 82x - 39x^2$ is the virial overdensity (Bryan & Norman 1998), $x \equiv \Omega_m / (\Omega_m + a^3 \Omega_{\Lambda}) - 1$, G is the gravitational constant, and $H(z)$ is the Hubble constant at some redshift z .

2.1 Star formation

Star formation is modelled based on a Schmidt law (Schmidt 1959),

$$\frac{d\rho_{\text{star}}}{dt} = \epsilon_{\text{ff}} \frac{\rho_{\text{gas}}}{t_{\text{ff}}}, \quad (1)$$

where ρ_{gas} is the density of gas, and $t_{\text{ff}} = \sqrt{3\pi/32G\rho_{\text{gas}}}$ is the free-fall time. The main parameter characterising star formation is

Table 1. Summary of simulation parameters.

Parameter	Value	Description
L_{box}	$2 \text{ Mpc } h^{-1}$	Simulation box size
Δx_{min}	0.7 pc	physical size of the finest cell
m_{DM}	$90 M_{\odot}$	mass resolution of DM particles
m_{star}	$91 M_{\odot}$	mass resolution of Pop II star particles
$\lambda_J/\Delta x$	32	Jeans length criterion for refinement
ϵ_{ff}	FK12	SF efficiency per free-fall time
N_{halo}	9	number of zoom-in haloes
IMF	Kroupa (2001)	(i.e., 1 SN per $91 M_{\odot}$)

the star formation efficiency per free-fall time (ϵ_{ff}). Local observations find that the efficiency is only a few percent when averaged over galactic scales (e.g., Kennicutt 1998). However, recent findings from small-scale numerical simulations suggest that ϵ_{ff} depends on physical properties of the ISM (Padoan & Nordlund 2011; Federrath & Klessen 2012). Motivated by this, we adopt a thermo-turbulent star formation model in which ϵ_{ff} is determined on a cell-by-cell basis (Devriendt et al. 2016, *in prep*). The details of the model will be presented elsewhere, and here, we briefly describe the basic idea for completeness.

The most fundamental assumption in the thermo-turbulent model is that the probability distribution function (PDF) of the density of a star-forming cloud is well described by a log-normal distribution. By integrating the gas mass from some critical density above which gas can collapse ($\rho = \rho(s_{\text{crit}})$) to infinity ($\rho = \infty$) per individual free-fall time, ϵ_{ff} can be estimated as (e.g., Federrath & Klessen 2012)

$$\epsilon_{\text{ff}} = \frac{\epsilon_{\text{ecc}}}{2\phi_t} \exp\left(\frac{3}{8}\sigma_s^2\right) \left[1 + \text{erf}\left(\frac{\sigma_s^2 - s_{\text{crit}}}{\sqrt{2}\sigma_s^2}\right)\right], \quad (2)$$

where $\sigma_s^2 = \ln(1 + b^2 \mathcal{M}^2)$ is the standard deviation of the logarithmic density contrast ($s \equiv \ln(\rho/\rho_0)$), ρ_0 is the mean density of gas, b is a parameter that depends on the mode of turbulence driving, $\epsilon_{\text{ecc}} \approx 0.5$ is the maximum fraction of gas that can accrete onto stars without being blown away by proto-stellar jets and outflows, $\phi_t \approx 0.57$ is a factor that accounts for the uncertainties in the estimation of a free-fall time of individual clouds, and \mathcal{M} is the sonic Mach number. We assume a mixture of solenoidal and compressive modes for turbulence ($b \approx 0.4$). An important quantity in Equation 2 is the critical density (s_{crit}), which may be regarded as the minimum density above which gas in the post-shock regions of a cloud is magnetically supercritical and thus can collapse (Krumholz & McKee 2005; Padoan & Nordlund 2011; Hennebelle & Chabrier 2011). Numerical simulations suggest that s_{crit} may be approximated as (Padoan & Nordlund 2011; Federrath & Klessen 2012)

$$s_{\text{crit}} = \ln(0.067\theta^{-2} \alpha_{\text{vir}} \mathcal{M}^2), \quad (3)$$

where θ is a numerical factor of order unity that encapsulates the uncertainty in the post-shock thickness with respect to the cloud size, and we adopt $\theta = 0.33$ that gives a best fit to the results of Federrath & Klessen (2012). Here $\alpha_{\text{vir}} \equiv 2E_{\text{kin}}/|E_{\text{grav}}|$ is the virial parameter of a cloud, which we take to be $\alpha_0 \approx 5(\sigma_{\text{gas}}^2 + c_s^2)/(\pi\rho_{\text{gas}}G\Delta x^2)$, where Δx is the size of a computational cell, c_s is the gas sound speed, and σ_{gas} is the turbulent gas velocity, which is the tracer of the velocity gradient. Note that the resulting ϵ_{ff} can be larger than 1 (Figure 1 of Federrath & Klessen 2012) if the sonic Mach number is very high ($\mathcal{M} \gtrsim 10$) in tightly gravitationally bound regions ($\alpha_{\text{vir}} \lesssim 0.1$). In practice, we find that

clouds with such conditions are extremely rare in our simulations, and ϵ_{ff} typically ranges from 5% to 20% when star particles are created.

This thermo-turbulent model allows for star formation only if the thermal plus turbulent pressure is not strong enough to prevent the gravitational collapse of a gas cloud. This may be characterised by the turbulent Jeans length (Bonazzola et al. 1987; Federrath & Klessen 2012)

$$\lambda_{\text{J,turb}} = \frac{\pi \sigma_{\text{gas}}^2 + \sqrt{36 \pi c_s^2 G \Delta x^2 \rho_{\text{gas}} + \pi^2 \sigma_{\text{gas}}^4}}{6 G \rho_{\text{gas}} \Delta x}. \quad (4)$$

In order for gas to be gravitationally unstable, the Jeans length needs to be smaller than the size of a computational cell ($\lambda_{\text{J,turb}} \leq \Delta$). Note that star formation occurs only in the maximally refined cells, because our refinement strategy enforces the thermal Jeans length to be resolved by 32 cells until it reaches the maximum level of refinement.

Once a potential site for star formation is identified, we estimate ϵ_{ff} using Equation (2) and determine the number of newly formed stars (N_*) based on a Poisson distribution

$$P(N_*) = \frac{\lambda^{N_*}}{N_*!} \exp(-\lambda), \quad (5)$$

with a mean of

$$\lambda = \epsilon_{\text{ff}} \frac{\rho_{\text{gas}} \Delta x^3}{m_{*,\text{min}}} \left(\frac{\Delta t_{\text{sim}}}{t_{\text{ff}}} \right), \quad (6)$$

where $m_{*,\text{min}}$ is the minimum mass of a star particle, and Δt_{sim} is the simulation integration time step. We adopt $m_{*,\text{min}} = 91 M_{\odot}$ for Pop II stars¹, which would host a single SN for a Kroupa initial mass function (Kroupa 2001). Of the stellar mass, 21 percent is returned to the surrounding medium as a result of SN explosions, and 1 percent is assumed to be newly synthesised to metals (i.e. a metal yield of 0.01).

The formation of Pop III stars is included following Wise et al. (2012b). We adopt a Salpeter-like IMF for masses above the characteristic mass (M_{char}), while the formation of low-mass Pop III stars is assumed to be inefficient,

$$\frac{dN}{d \log M} \propto M^{-1.3} \exp \left[- \left(\frac{M_{\text{char}}}{M} \right)^{1.6} \right], \quad (7)$$

where N is the number of Pop III stars per logarithmic mass bin. The precise determination of the characteristic mass is a matter of debate. Early studies suggested that the mass of protostellar clumps is $\sim 100 M_{\odot}$ (Abel et al. 2002; Bromm et al. 2002; Yoshida et al. 2006). Later, several groups point out that gas clumps may be fragmented further reducing the characteristic mass to $\sim 40 M_{\odot}$ (Turk et al. 2009; Greif et al. 2012). However, recent radiation-hydrodynamics simulations report that several tens to a thousand solar masses of gas may collapse to form a Pop III star (Hirano et al. 2014; Hosokawa et al. 2015, c.f., Lee & Yoon 2016). In this work, we adopt $M_{\text{char}} = 100 M_{\odot}$, consistent with the most recent simulations.

We assume that Pop III stars form only in a region where the gas metallicity is below $10^{-6} Z_{\odot}$. This means that at least one Pop III star will form in a dark matter halo during the initial gas collapse due to radiative cooling by molecular hydrogen. In principle,

the external pollution by neighbouring haloes can suppress the formation of Pop III stars (e.g. Smith et al. 2015), but our simulated haloes are chosen to reside in an isolated environment and thus are not affected by neighbours. Note that more than one Pop III star can form in each halo if the first Pop III star does not explode and enrich the IGM/ISM or if a pristine gas cloud is accreted onto a dark matter halo through halo mergers.

2.2 Stellar feedback

Modelling the feedback from stars is essential to predict the escape of LyC photons in dwarf galaxies. In order for LyC photons to leave their host dark matter halo, feedback should clear away low-density channels or entirely blow out the birth clouds. Otherwise, the photons will simply be absorbed by neutral hydrogen inside of the halo. We include three different types of feedback (photoionisation, radiation pressure from the absorption of UV and IR photons, and Type II supernova feedback) in our simulations.

2.2.1 Radiation feedback

Young, massive stars emit large amounts of ionising photons, which drive winds through various processes. Because the absorption cross section of neutral hydrogen is so large ($\sigma_{\text{abs}} \sim 6 \times 10^{-18} \text{ cm}^2$), the presence of a small amount of hydrogen makes the ISM optically thick to photons with $E > 13.6 \text{ eV}$. When the ISM is fully ionised, dust becomes the next most efficient absorber, as its opacity in the UV wavelengths is large as well ($\kappa_{\text{abs}} \sim 1000 \text{ cm}^2/\text{g}$).

Of the several radiation feedback processes, photoionisation is probably the most important mechanism that governs the dynamics of a giant molecular cloud (GMC, Lopez et al. 2014; Dale et al. 2014; Rosdahl & Teyssier 2015). LyC photons can ionise hydrogen, which heat the gas to $T \approx 2 \times 10^4 \text{ K}$. This creates an over-pressurised HII bubble that lowers the density of the ambient medium and drives winds with velocities up to 10 km s^{-1} (e.g. Krumholz et al. 2007; Walch et al. 2012; Dale et al. 2014). To capture the dynamics of the HII region, the Stromgren sphere radius (r_{S}) should be resolved.

$$r_{\text{S}} = \left(\frac{3 \dot{N}_{\text{p}}}{4 \pi \alpha_{\text{B}} n_{\text{H}}^2} \right)^{1/3} \approx 1.2 \text{ pc} \left(\frac{m_{\text{star}}}{10^3 M_{\odot}} \right)^{1/3} \left(\frac{n_{\text{H}}}{10^3 \text{ cm}^{-3}} \right)^{-2/3}, \quad (8)$$

where \dot{N}_{p} is the production rate of ionising photons, and $\alpha_{\text{B}} = 2.6 \times 10^{-13} \text{ cm}^3 \text{ s}^{-1}$ is the case B recombination rate coefficient at $T = 10^4 \text{ K}$. For the latter equality, we use $N_{\text{p}} = 5 \times 10^{46} \text{ s}^{-1}$ per $1 M_{\odot}$. Note that this scale describes the maximum distance within which recombination is balanced by ionisation assuming that photo-heating does not affect the dynamics of the ISM.

When ionising photons are absorbed by the neutral ISM, their momentum is transferred to the medium (e.g., Haehnelt 1995) at a rate

$$\dot{p}_{\gamma} = \sum_i^{\text{groups}} \frac{\mathbf{F}_i}{c} \left(\kappa_i + \sum_j^{\text{HI, HeI, HeII, LW}} \sigma_{ij} n_j \right), \quad (9)$$

where \mathbf{F}_i is the photon flux ($\text{erg cm}^{-2} \text{ s}^{-1}$) for i -th photon group, κ is the dust opacity ($\text{cm}^2 \text{ g}^{-1}$), σ is the photoionisation cross-section (cm^2), and n_j is the number density (cm^{-3}) of the ion species j . For a Kroupa IMF, direct radiation pressure from ionising radiation

¹ We discuss the possible impact of the IMF sampling, the neglect of run-away stars, and the uncertainties in stellar evolutionary models on the determination of the escape fractions in Section 4.3.

($\lambda \leq 912\text{\AA}$) can impart momentum of up to $\sim 40 \text{ km s}^{-1} M_{\odot}$ if we integrate the number of ionising photons from a simple stellar population of $1 M_{\odot}$ until 50 Myr (Leitherer et al. 1999). The absorption of non-ionising UV and optical photons by dust can further increase the total momentum input to $\sim 190 \text{ km s}^{-1} M_{\odot}$ within 50 Myr.

We also take into account radiation pressure by trapped infrared (IR) photons. IR photons are generated when UV and optical photons are absorbed by dust or when molecular hydrogen is fluorescently excited by absorption of Lyman-Werner photons and radiatively de-excited through forbidden rotational-vibrational transitions (see the Chemistry section). We assume that these IR photons are efficiently trapped only if the optical depth over the cell width by dust is high. The resulting trapped IR photon energy in each cell is modelled as (Rosdahl & Teyssier 2015)

$$E_{\text{IR, trapped}} = f_{\text{trapped}} E_{\text{IR}} = \exp\left(-\frac{2}{3\tau_d}\right) E_{\text{IR}} \quad (10)$$

where $\tau_d = \kappa_{\text{sc}} \rho_{\text{gas}} \Delta x$ and $\kappa_{\text{sc}} \sim 5 (Z_{\text{gas}}/Z_{\odot}) \text{ cm}^2/\text{g}$ is the scattering cross-section by dust (Semenov et al. 2003). This trapped IR radiation is then included as a non-thermal pressure term in the momentum equation, as

$$\frac{\partial \rho \mathbf{v}}{\partial t} + \nabla \cdot (\rho \mathbf{v} \otimes \mathbf{v} + (P + P_{\text{rad}}) \mathbf{I}) = \dot{\mathbf{p}}_{\gamma} + \rho \nabla \Phi \quad (11)$$

where

$$P_{\text{rad}} = \frac{\tilde{c} E_{\text{IR, trapped}}}{c} \quad (12)$$

The non-thermal pressure imparted by trapped IR radiation (P_{rad}) is also added to the energy equation. Note that these trapped IR photons are advected with the gas, while the remaining fraction of the IR energy density

$$E_{\text{IR, stream}} = \left[1 - \exp\left(-\frac{2}{3\tau_d}\right)\right] E_{\text{IR}} \quad (13)$$

is diffused out to the neighbouring cells and it is re-evaluated whether or not these photons are trapped by dust (Rosdahl & Teyssier 2015).

In this paper, we adopt the photon production rates of Pop II stars from Bruzual & Charlot (2003) assuming a Kroupa IMF. This is done by interpolating the spectral energy distributions for a given metallicity and age and by counting the LyC photons from the spectrum of each star particle. The lifetime and the photon production rates for Pop III stars are taken by fitting the results of Schaerer (2002).

2.2.2 Type II SN explosions

We adopt the mechanical feedback scheme introduced by Kimm & Cen (2014) and Kimm et al. (2015) to model the explosion of massive ($M \geq 8 M_{\odot}$) Pop II stars. Based on Thornton et al. (1998, see also Blondin et al. 1998; Kim & Ostriker 2015; Geen et al. 2015; Martizzi et al. 2015), this model captures the correct radial momentum input from SN explosions at the snowplough phase ($p_{\text{SN, snow}}$),

$$p_{\text{SN, snow}} = 3 \times 10^5 \text{ km s}^{-1} M_{\odot} n_{\text{H}}^{-2/17} E_{51}^{16/17} Z'^{-0.14}, \quad (14)$$

by imparting momentum according to the stage of the Sedov-Taylor blast wave. Here n_{H} is the hydrogen number density in units of cm^{-3} , E_{51} is the explosion energy in units of 10^{51} erg , and $Z' = \max[0.01, Z/0.02]$ is the metallicity of gas, normalised to the solar value.

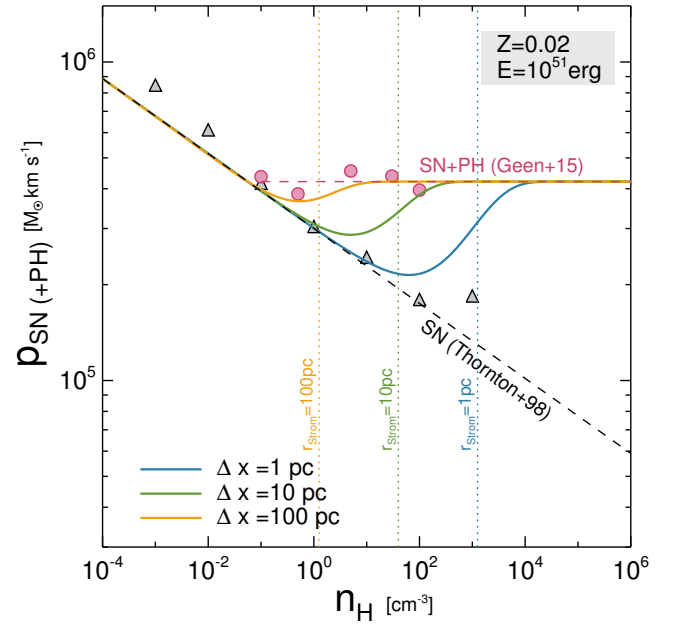


Figure 1. Final radial momentum from an individual SN explosion in different environments (p_{SN}). Grey triangles represent the results from 1D hydrodynamic calculations (Thornton et al. 1998), while violet circles show the final momentum in the presence of ionising radiation from 3D radiation-hydrodynamic simulations (Geen et al. 2015). The grey and violet dashed lines display a simple fit to these results ($p_{\text{SN}} \propto n_{\text{H}}^{-2/17}$, $p_{\text{SN}} \sim \text{const}$), respectively. The inclusion of photo-heating enhances p_{SN} by reducing the density of the ambient medium before SNe explode and also by imparting momentum from photo-heating and direct radiation pressure. We take this effect into consideration explicitly only if the Stromgren sphere is unresolved in our simulations. When the Stromgren sphere is resolved, the effect is captured self-consistently in our simulations. The solid lines with different colours illustrate three examples of the momentum that we would impart during the momentum-conserving phase at different resolutions in the presence of the radiation from a star cluster with $M_{\text{star}} = 10^3 M_{\odot}$, and the dotted lines indicate the corresponding densities at which the Stromgren sphere becomes unresolved. Notice that we inject momentum of the initial ejecta ($p_{\text{SN, ad}} = 4.5 \times 10^4 M_{\odot} \text{ km s}^{-1}$) if the mass in the neighbouring cells is negligible compared to the ejecta mass (see Equation 21).

Recently, Geen et al. (2015) have shown that the final radial momentum from a SN can be augmented by including photoionisation from massive stars. Because the thermal energy that is liberated during the ionisation process over-pressurises and decreases the density of the surroundings into which SNe explode, the final momentum from SNe in a medium pre-processed by ionising radiation is found to be significantly larger than without it. Most notably, they find that the amount of momentum is nearly independent of the background density, indicating that more radial momentum should be imparted to the ISM than suggested by Thornton et al. (1998), especially when SNe explode in dense environments. In principle, this extra momentum should be generated by solving the full radiation hydrodynamics, but this requires the simulation to resolve the Stromgren radius. If young stars are embedded in a cloud denser than 10^3 cm^{-3} , the effect of photoionisation is likely to be underestimated with our pc scale resolution. In order to circumvent this issue, we adopt a simple fit to the results of Geen et al. (2015),

$$p_{\text{SN+PH}} = 4.2 \times 10^5 \text{ km s}^{-1} M_{\odot} E_{51}^{16/17} Z'^{-0.14}, \quad (15)$$

if the Stromgren sphere is under-resolved ($\Delta x \gg r_S$). We adopt the dependence on the SN energy and the metallicity from [Thorn-ton et al. \(1998\)](#). Note that the values taken from [Geen et al. \(2015\)](#) are lowered by a factor $1.2^{16/17}$, as they use a 20% larger SN explosion energy (1.2×10^{51} erg) compared to other studies ([Thorn-ton et al. 1998](#)). The final momentum input during the snowplough phase is then taken from the combination of $p_{\text{SN,snow}}$ and $p_{\text{SN+PH}}$ by comparing the resolution of a computational cell (Δx) with the Stromgren radius (r_S), as

$$p_{\text{SN}} = p_{\text{SN,snow}} \exp\left(-\frac{\Delta x}{r_S}\right) + p_{\text{SN+PH}} \left(1 - \exp\left[-\frac{\Delta x}{r_S}\right]\right). \quad (16)$$

Figure 1 illustrates three examples of the SN momentum that we would inject at different resolutions (1, 10, and 100 pc) as a function of density in the presence of the radiation from a star cluster with $10^3 M_\odot$.

Specifically, the model first calculates the mass ratio (χ) between the swept-up mass (M_{swept}) and the ejecta mass (M_{ej}) along each $N_{\text{nb}}^{\text{bor}}$ neighbouring cell, as

$$\chi \equiv dM_{\text{swept}}/dM_{\text{ej}}, \quad (17)$$

where

$$dM_{\text{ej}} = (1 - \beta_{\text{sn}})M_{\text{ej}}/N_{\text{nb}}^{\text{bor}}, \text{ and} \quad (18)$$

$$dM_{\text{swept}} = \rho_{\text{nb}}^{\text{bor}} \left(\frac{\Delta x}{2}\right)^3 + \frac{(1 - \beta_{\text{sn}})\rho_{\text{host}}\Delta x^3}{N_{\text{nb}}^{\text{bor}}} + dM_{\text{ej}}. \quad (19)$$

Here β_{sn} is a parameter that determines what fraction of the gas mass ($M_{\text{ej}} + \rho_{\text{host}}\Delta x^3$) is re-distributed to the host cell of a SN. In order to distribute the mass evenly to the host and neighbouring cells in the uniformly refined case, we take $\beta_{\text{sn}} = 4/52$. Note that since the maximum number of neighbouring cells is 48 if they are more refined than the host cell of a SN (see Figure 15 of [Kimm & Cen \(2014\)](#)), we use $N_{\text{nb}}^{\text{bor}} = 48$. If the neighbours are not further refined, we simply take the physical properties (ρ , \vec{v} , Z) of the neighbours assuming that they are refined.

We then use the mass ratio (χ) to determine the phase of the Sedov-Blast wave. To do so, we define the transition mass ratio (χ_{tr}) by equating p_{SN} with the radial momentum one would expect during the adiabatic phase $p_{\text{ad}} = \sqrt{2\chi M_{\text{ej}} f_e E_{\text{SN}}}$, where $f_e \sim 2/3$ is the fraction of energy that is left in the beginning of the snowplough phase, as

$$\chi_{\text{tr}} \approx \frac{900 n_{\text{H}}^{-4/17} E_{51}^{-2/17} Z^{1-0.28}}{f_e (M_{\text{ej}}/M_\odot)}. \quad (20)$$

If χ is greater than χ_{tr} , we inject the momentum during the snowplough phase, whereas the momentum during the adiabatic phase is added to the neighbouring cell, as

$$p_{\text{SN}} = \begin{cases} p_{\text{SN,ad}} = \sqrt{2\chi M_{\text{ej}} f_e(\chi) E_{\text{SN}}} & (\chi < \chi_{\text{tr}}) \\ p_{\text{SN}} & (\chi \geq \chi_{\text{tr}}) \end{cases}, \quad (21)$$

where the fraction of energy left in the SN bubble ($f_e(\chi) \equiv 1 - \frac{\chi-1}{3(\chi_{\text{tr}}-1)}$) is modified to smoothly connect the two regimes.

In order to account for the fact that the lifetime of supernova progenitors varies from 3 Myr to 40 Myr depending on their mass, we randomly draw the lifetime based on the integrated SN occurrence rate from Starburst99 ([Leitherer et al. 1999](#)) using the inverse method, as in the MFBmp model from [Kimm et al. \(2015\)](#).

Table 2. Properties of photon groups.

Photon group	ϵ_0 [eV]	ϵ_1 [eV]	κ [cm ² /g]	Main function
IR	0.1	1.0	5	Radiation pressure (RP)
Optical	1.0	5.6	10^3	Direct RP
FUV	5.6	11.2	10^3	Photoelectric heating
LW	11.2	13.6	10^3	H ₂ dissociation
EUV _{HI,1}	13.6	15.2	10^3	HI ionisation
EUV _{HI,2}	15.2	24.59	10^3	HI and H ₂ ionisation
EUV _{HeI}	24.59	54.42	10^3	HeI ionisation
EUV _{HeII}	54.42	∞	10^3	HeII ionisation

2.2.3 Explosion of Pop III stars

The explosions of Pop III stars are modelled similarly as Pop II explosions, but with different energy and metal production rates. Stars with $40 M_\odot \leq M_\star \leq 120 M_\odot$ and $M_\star \geq 260 M_\odot$ are likely to implode without releasing energy and metals, while massive stars with $120 M_\odot < M_\star < 260 M_\odot$ may end up as a pair-instability SN ([Heger et al. 2003](#)). The explosions of stars less massive than $40 M_\odot$ are modelled as either normal Type II SN with 10^{51} erg if $11 M_\odot \leq M_\star \leq 20 M_\odot$ ([Woosley & Weaver 1995](#)) or hypernova if $20 M_\odot \leq M_\star \leq 40 M_\odot$ ([Nomoto et al. 2006](#)). For the explosion energy ($E_{\text{SN,III}}$) and returned metal mass (M_z), we adopt the compilation of [Wise et al. \(2012a\)](#), which is based on [Woosley & Weaver \(1995\)](#); [Heger & Woosley \(2002\)](#); [Nomoto et al. \(2006\)](#), as

$$\frac{E_{\text{SN,III}}}{10^{51} \text{ erg}} = \begin{cases} 1 & [11 \leq M_\star < 20] \\ (-13.714 + 1.086 M_\star) & [20 \leq M_\star \leq 40] \\ (5.0 + 1.304 \times (M_{\text{He}} - 64)) & [140 \leq M_\star \leq 230] \\ 0 & \text{elsewhere} \end{cases}, \quad (22)$$

where $M_{\text{He}} = \frac{13}{24}(M_\star - 20)$ is the helium core mass, and

$$\frac{M_z}{M_\odot} = \begin{cases} 0.1077 + 0.3383 (M_\star - 11) & [11 \leq M_\star < 20] \\ -2.7650 + 0.2794 M_\star & [20 \leq M_\star \leq 40] \\ (13/24) (M_\star - 20) & [140 \leq M_\star \leq 230] \\ 0 & \text{elsewhere} \end{cases}. \quad (23)$$

We neglect accretion and feedback from black holes formed by the implosion of massive Pop III stars.

2.3 Non-equilibrium photo-chemistry and radiative cooling

The public version of RAMSES-RT can solve non-equilibrium chemistry of hydrogen and helium species (HI, HII, HeI, HeII, HeIII, and e⁻), involving collisional excitation, ionisation, and photoionisation ([Rosdahl et al. 2013](#)). In order to take into account cooling by molecular hydrogen (H₂), which is essential to model gas collapse in mini-haloes, we have made modifications based on [Glover et al. \(2010\)](#) and [Baczynski et al. \(2015\)](#). Note that the photon number density and fluxes in the eight energy bins that we describe in Table 2 are computed in a self-consistent way by tracing the photon fluxes from each star particle. The chemical reactions and radiative cooling are fully coupled with the eight photon groups. More details of the photo-chemistry will be presented in [Katz et al. \(2016\)](#) in terms of the prediction of molecular hydrogen in high-z galaxies.

Molecular hydrogen mainly forms on the surface of interstellar dust grains. However, in the early universe where there is little dust (e.g., [Fisher et al. 2014](#)), the formation is dominated by the reaction involving H^- . These hydrogen molecules are dissociated by Lyman-Werner photons with energy $11.2 \text{ eV} \leq E \leq 13.6 \text{ eV}$ or collisions with other species (HI , H_2 , HeI , and e^-). Furthermore, H_2 can be ionised by photons with $E \geq 15.2 \text{ eV}$. We assume that all H_2^+ is immediately destroyed by dissociative recombination. To estimate the formation rate of molecular hydrogen through the H^- channel, we assume that the abundance of H^- is set by the equilibrium between the formation and destruction via associative detachment and mutual neutralisation (e.g., [Anninos et al. 1997](#)), as

$$k_1 n_{\text{HI}} n_e = k_2 n_{\text{H}} - n_{\text{HI}} + k_5 n_{\text{H}} - n_{\text{HII}} + k_{13} n_{\text{H}} - n_e, \quad (24)$$

where k_X is the reaction rate (reactions 1, 2, 5, and 13 in Appendix B of [Glover et al. 2010](#)). This neglects the photo-detachment of H^- by infrared photons, and it may thus lead to the over-estimation of the H^- abundance when Pop II stars are present ([Cen 2016](#)). However, we expect that cooling is dominated by metals once Pop III stars explode (see Figure 2 of [Wise et al. 2014](#), for example), hence the gas collapse in mini-haloes is unlikely to be significantly affected.

Radiative cooling by hydrogen and helium species is directly computed from the chemical network. In particular, we include the cooling by molecular hydrogen following [Halle & Combes \(2013\)](#), which is largely based on [Hollenbach & McKee \(1979\)](#). In addition, Lyman Werner photons also heat the gas when they photo-dissociate and photo-ionise H_2 or when they indirectly excite the vibrational levels of H_2 (see section 2.2.4 in [Baczynski et al. 2015](#)). Gas can cool further with the aid of metals, which we consider by interpolating look-up tables which are pre-computed with the Cloudy code ([Ferland et al. 1998](#)) as a function of density, temperature, and redshift ([Smith et al. 2011](#)). Finally, we also include photoelectric heating on dust by UV photons with $5.6 \text{ eV} \leq h\nu \leq 13.6 \text{ eV}$ ([Bakes & Tielens 1994](#)) following [Baczynski et al. \(2015, Section 2.2.5\)](#), as

$$\mathcal{H}_{\text{pe}} = 1.3 \times 10^{-24} \epsilon G_0 f_{\text{D/G}} n_{\text{H}} [\text{erg cm}^{-3} \text{ s}^{-1}], \quad (25)$$

where G_0 is the strength of the local intensity in each cell, normalised to the Habing field ($1.6 \times 10^{-3} \text{ erg s}^{-1} \text{ cm}^{-2}$, [Habing 1968](#)), and $f_{\text{D/G}} = 1$ is the dust-to-gas ratio, normalised to the local ISM value ([Draine et al. 2007](#)). The efficiency for the heating (ϵ) is taken from [Wolfire et al. \(2003\)](#), as

$$\epsilon = \frac{4.9 \times 10^{-2}}{1 + 4.0 \times 10^{-3} (G_0 T^{1/2} / n_e \phi_{\text{PAH}})^{0.73}} \frac{3.7 \times 10^{-2} (T/10^4)^{0.7}}{1 + 2.0 \times 10^{-4} (G_0 T^{1/2} / n_e \phi_{\text{PAH}})}, \quad (26)$$

where $\phi_{\text{PAH}} = 0.5$ is a factor that controls the collision rates between electron and PAH. We do not use any uniform UV or Lyman Werner background radiation (e.g., [Haardt & Madau 2012](#)).

3 RESULTS

The main aim of this paper is to assess the contribution of mini-haloes to the reionisation history of the universe. For this purpose, we investigate the evolution of nine dwarf galaxies in haloes of mass $10^6 \text{ M}_\odot \lesssim M_{\text{vir}} \lesssim 10^8 \text{ M}_\odot$ at $7 \leq z \leq 20$. In this section, we first describe the main features of the simulated galaxies, present

the escape fraction of LyC photons at the virial radius, and discuss the physical processes governing the evolution of the escape fraction.

3.1 Galactic properties of the dwarf population during reionisation

Our simulated haloes begin forming Pop III stars when the halo mass approaches a few times 10^6 M_\odot . These Pop III stars disperse dense gas clouds and pollute the ISM and IGM with metals via energetic explosions. We find that the typical metallicity of the halo gas after the explosion of Pop III stars is $\sim 10^{-3} - 10^{-2} Z_\odot$, consistent with previous studies ([Greif et al. 2010](#); [Ritter et al. 2012](#)). The enrichment of the dense medium ($n_{\text{H}} \geq 100 \text{ cm}^{-3}$) takes place more slowly than for the IGM ($\sim 10^{-4} - 10^{-3} Z_\odot$), as this gas mixes with the newly accreted, pristine material with primordial composition. Once the metal-enriched gas collapses, Pop II stars form in a very stochastic fashion. As the haloes become massive ($\sim 10^8 \text{ M}_\odot$) and a large amount of gas accumulates in the halo centres, the star formation histories become less bursty, compared to those in haloes with masses of a few times 10^7 M_\odot . Because stellar feedback violently disrupts star-forming clouds, the gas component of these mini-haloes show irregular morphologies rather than well-defined disks (Figure 2). The resulting stellar metallicities in haloes with $\sim 10^8 \text{ M}_\odot$ range from $Z = 10^{-3} Z_\odot$ to $Z = 10^{-1.7} Z_\odot$ with a median of $Z = 10^{-2.6} Z_\odot$. We summarise several galactic properties in the nine simulated haloes in Table 3.

Overall, we find that *star formation is very inefficient in the mini-haloes* (Figure 4). For example, haloes with masses $\sim 10^{7.5} \text{ M}_\odot$ form clusters of stars of $\sim 10^{3-4} \text{ M}_\odot$. At larger masses ($M_{\text{vir}} \sim 10^8 \text{ M}_\odot$), the efficiency becomes higher, but still $\lesssim 1\%$ of baryons are converted into stars. We note that these results are consistent with the recent radiation-hydrodynamic calculations of [Wise et al. \(2014\)](#); [Xu et al. \(2016\)](#). However, our results are slightly different from these studies in the sense that the least massive haloes ($M_{\text{vir}} \lesssim 10^7 \text{ M}_\odot$) appear to host progressively smaller amount of stars, whereas, in [Wise et al. \(2014\)](#), the stellar mass appears to saturate at a few times 10^3 M_\odot . We also find that the dispersion in the stellar mass-halo mass relation is smaller than that of [Xu et al. \(2016\)](#). This is likely to be due to the small number of samples used in this work. Indeed, [Xu et al. \(2016\)](#) find a larger dispersion than [Wise et al. \(2014\)](#) when they increase the number of galaxies from 32 to ~ 2000 simulated with the same assumptions.

The inefficient star formation in our simulations is due to strong stellar feedback. This can be inferred from Figure 3 where the star formation histories are shown to be very bursty. The typical time scale of star formation does not exceed $\sim 10 \text{ Myr}$ and is often smaller than 5 Myr when the halo mass is small. The recovery time after a burst of star formation in the mini-haloes is also large, ranging from $\sim 20 \text{ Myr}$ to $\sim 200 \text{ Myr}$. Because radiation can drive winds by over-pressurising the ISM and early SNe can create cavities in the star-forming regions, we find that the majority of SNe explode in a low-density environment with $n_{\text{H}} \sim 2 \times 10^{-3} \text{ cm}^{-3}$, while stars form only in very dense environments with $n_{\text{H}} \geq 4 \times 10^4 \text{ cm}^{-3}$ (Figure 5).

At present, there are no direct observational constraints on the evolution of galaxies in mini-haloes at high redshift, and thus it is not currently possible to validate our feedback model. Nevertheless, it is worth noting that the simulated galaxies follow the stellar mass-to-halo mass sequence obtained from [Kimm & Cen \(2014\)](#) (Figure 4), which successfully reproduces the faint-end slope and

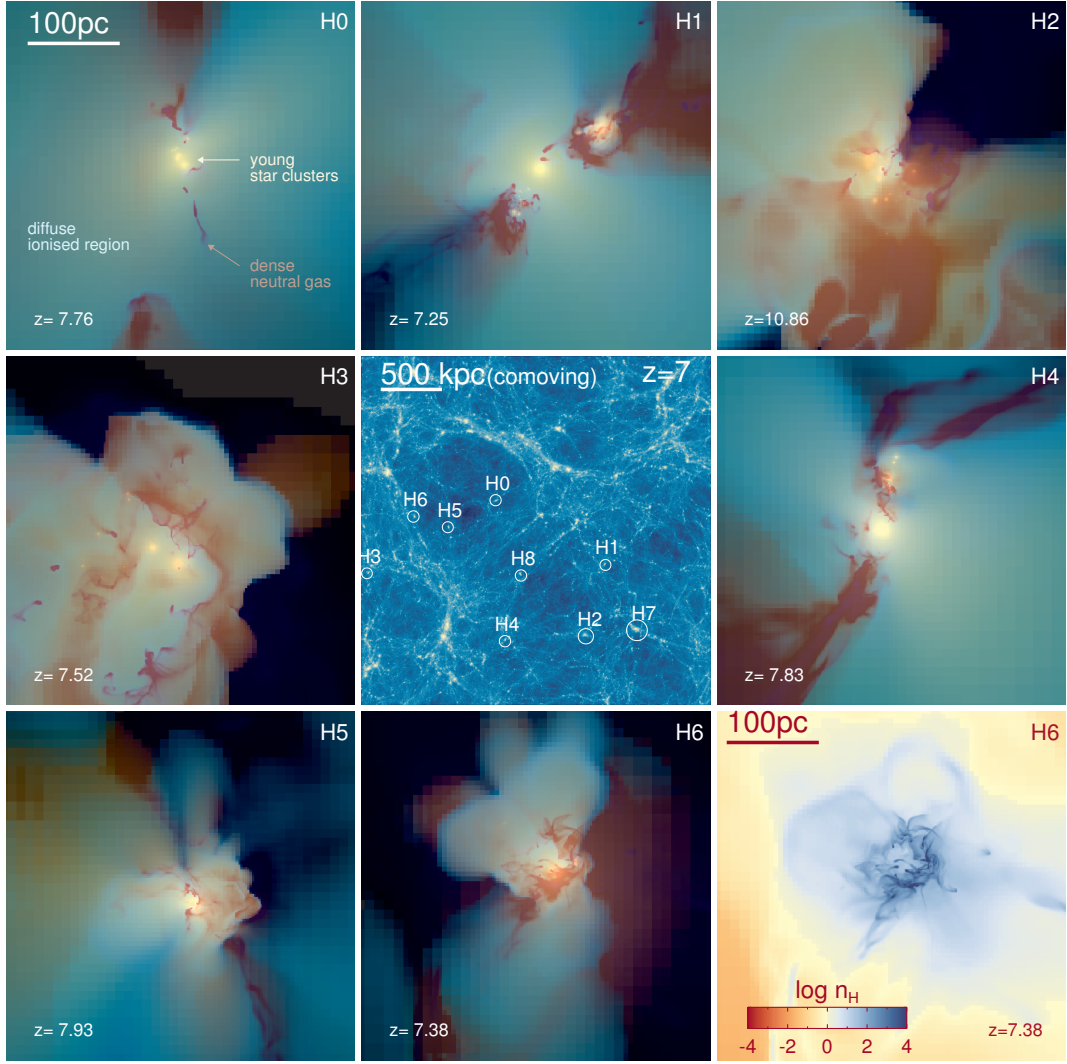


Figure 2. Composite images of the density, HII fraction, and HI-ionising photon density for seven simulated haloes out of the total nine sample. The central panel displays the location of the nine zoom-in haloes in the entire simulation box of length 2 Mpc h^{-1} (comoving) at $z = 7$. We evolve each halo until its mass becomes large enough ($M_{\text{halo}} \approx 10^8 M_{\odot}$) to radiate energy away mainly by atomic transitions. Actively star-forming regions are shown as bright yellow colours, while highly ionised regions are displayed as light blue colours. Dark regions show mostly neutral gas. It can be seen that the central star-forming clump is disrupted by stellar feedback in many cases, leading to a high escape fraction of LyC photons. The bottom right most panel shows the projected gas density distribution of the H6 halo for comparison.

Table 3. Summary of simulation results. All quantities are measured at the final redshift of each simulation. Column (1): ID of simulated halo. Column (2): virial mass of the dark matter halo. Column (3): total stellar mass of Pop II. Column (4): total gas mass inside a halo. Column (5): mass-weighted mean metallicity of star particles. Column (6): mass-weighted mean gas metallicity inside a halo. Column (7): total stellar mass of Pop III. Column (8): initial redshift to form Pop III stars. Column (9): initial redshift to form Pop II stars. Column (10): final redshift of each simulation.

Halo ID	$\log M_{\text{halo}}$ [M_{\odot}]	$\log M_{\text{star,II}}$ [M_{\odot}]	$\log M_{\text{gas}}$ [M_{\odot}]	$\langle \log Z_{\text{star}} \rangle$ [Z_{\odot}]	$\log Z_{\text{gas}}$ [Z_{\odot}]	$\log M_{\text{star,III}}$ [M_{\odot}]	z_{PopIII}	z_{PopII}	z_{final}
H0	8.05	4.53	6.93	-3.0	-2.7	3.20	12.4	10.6	7.0
H1	8.03	5.17	7.10	-2.8	-2.4	1.57	14.3	12.7	7.3
H2	8.08	5.26	7.06	-2.5	-2.0	3.35	18.1	15.0	10.6
H3	8.00	5.08	7.16	-2.7	-2.5	1.40	10.9	10.0	7.5
H4	8.03	4.72	6.32	-2.8	-2.6	3.50	14.7	13.4	7.0
H5	8.01	5.17	6.98	-2.7	-2.3	3.31	14.7	13.6	8.1
H6	7.96	5.70	7.17	-2.4	-2.0	2.16	15.6	13.8	7.3
H7	7.91	4.61	7.09	-3.0	-2.9	2.69	13.4	12.4	11.2
H8	7.85	4.17	7.00	-3.3	-3.2	1.59	12.5	10.7	8.1

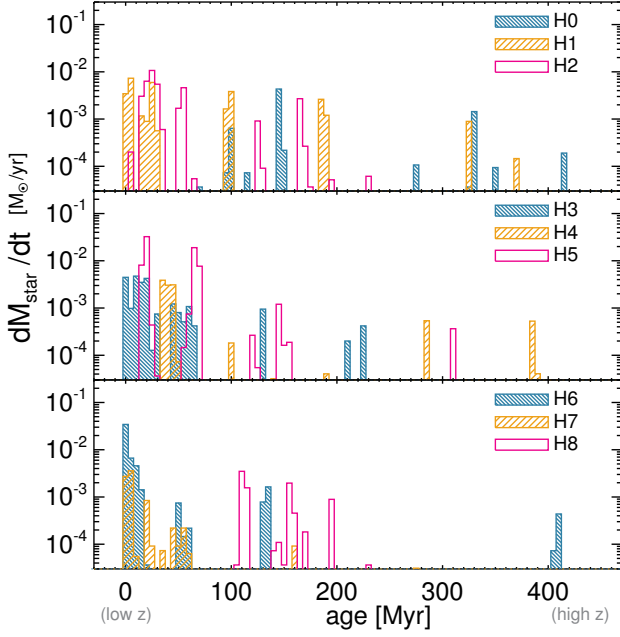


Figure 3. Star formation histories of the dwarf galaxies in our simulated mini-haloes. The x-axis indicates the age of stars measured at the end of each simulation. Different colour coding denotes different galaxies. We split the sample for clarity. It can be seen that star formation is very stochastic. The recovery time from the stellar feedback ranges from $\sim 20 - 200$ Myr.

normalisation of the observed UV luminosity function at $z \sim 7$ without dust correction. It is also interesting to note that the predicted stellar masses are comparable to the *local* stellar mass-to-halo mass relation derived from the abundance matching technique (Behroozi et al. 2013) when extrapolated to the mini-halo mass regime. The fact that the simulated galaxies are very metal-poor ($\sim 0.003 Z_{\odot}$) suggests that our results do not suffer from the over-cooling problem, as it usually leads to significantly higher metallicities of $\gtrsim 0.1 Z_{\odot}$ (Wise et al. 2012a).

Our simulated galaxies are slightly more metal-poor (roughly a factor of two) than the local dwarf population (Woo et al. 2008). However, given the large scatter in the observed stellar metallicities, the difference is unlikely to be significant. Rather, we find that the simulated protogalaxies are more compact (by a factor of a few) than the local dwarf spheroids of comparable masses (e.g., Brodie et al. 2011). As can be observed in Figure 2, the stellar components of high- z dwarves are dominated by a few clusters, and the resulting half-mass radii are found to be ~ 20 -100 pc. The smaller size of the simulated galaxies may not be very surprising, given that the universe is denser and star formation per unit stellar mass is known to be more efficient at high redshifts (e.g., Speagle et al. 2014).

3.2 Escape Fraction of LyC photons

We calculate the escape fraction by comparing the photon flux (F_{ion}) at the virial radius with the emergent flux from stars. Since photons travel with finite speed, we use the production rate at $t - R_{\text{vir}}/\tilde{c}$, where the time delay (R_{vir}/\tilde{c}) is roughly ~ 1 Myr. The escape fraction is then

$$f_{\text{esc}}(t) = \frac{\int d\Omega \vec{F}_{\text{ion}}(t) \cdot \hat{r}}{\int dm_{\star} \dot{N}_{\text{ion}}(t - R_{\text{vir}}/\tilde{c})}, \quad (27)$$

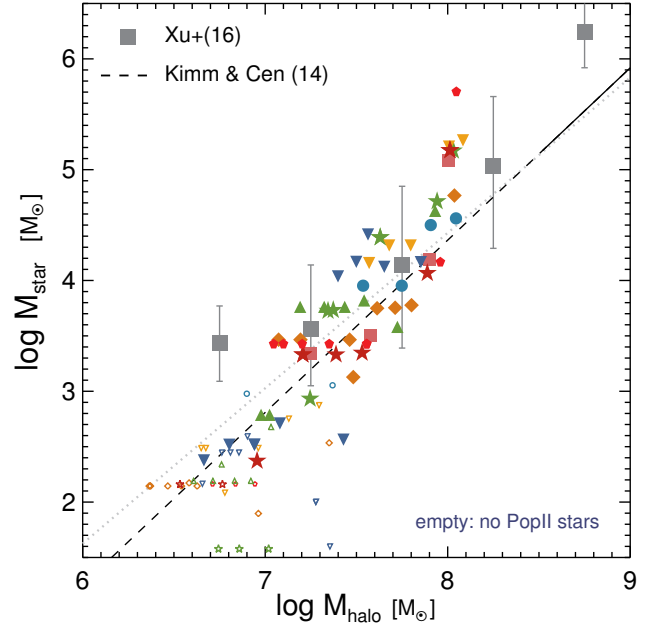


Figure 4. Predicted stellar mass as a function of halo mass in our simulations. Different colour codings and symbols correspond to nine different haloes. Note that we plot the results at various redshifts, and thus this may also be seen as an evolutionary sequence at $7 \leq z < 18$. The empty symbols indicate the haloes hosting only Pop III stars, while the haloes with Pop II stars are shown as filled symbols. We also include the stellar mass in haloes outside the main halo if they are still within the zoom-in region and not contaminated by coarse dark matter particles. We find that our results follow the slope and normalisation predicted by Kimm & Cen (2014) (black line) which reproduced the UV luminosity function at $z \sim 7$. The dashed line indicates an extrapolation of the Kimm & Cen (2014) results. Our results are also in fair agreement with simulations from Xu et al. (2016) (the grey squares). For comparison, we include the empirical sequence at $z \approx 0$ extrapolated to the mini-halo regime (Behroozi et al. 2013) (grey dotted line).

where Ω is the solid angle, m_{\star} is the mass of star particles, \dot{N}_{ion} is the production rate of ionising radiation per unit mass. Note that the choice of the radius (i.e., R_{vir}) at which the measurement is made is conventional, but it is desirable to measure the escape fraction at a radius large enough that it can be combined with estimates of the clumping factor from large-scale simulations (e.g., Pawlik et al. 2009; Finlator et al. 2012; Shull et al. 2012; So et al. 2014) to study the reionisation history of the universe.

3.2.1 A High Average Escape Fraction in mini-haloes

Figure 6 shows that LyC photons escape from mini-haloes quite efficiently after a burst of star formation. Not only Pop III stars, which are characterised by a constant photon production rate and an abrupt decrease, but also Pop II stars, characterised instead by an exponentially decaying rate, show a high escape fraction of $f_{\text{esc}} \sim 30 - 40\%$. In some cases, the escape fraction remains very low even after the formation of Pop II star clusters. Similarly, not all Pop III stars lead to a high escape fraction. Figure 7 displays the photon-number weighted escape fraction of individual Pop III stars with different masses. It can be seen that only massive Pop III stars with $M_{\text{PopIII}} \gtrsim 100 M_{\odot}$ are able to provide LyC photons to the IGM (Whalen et al. 2004), while almost all of the ionising radiation from

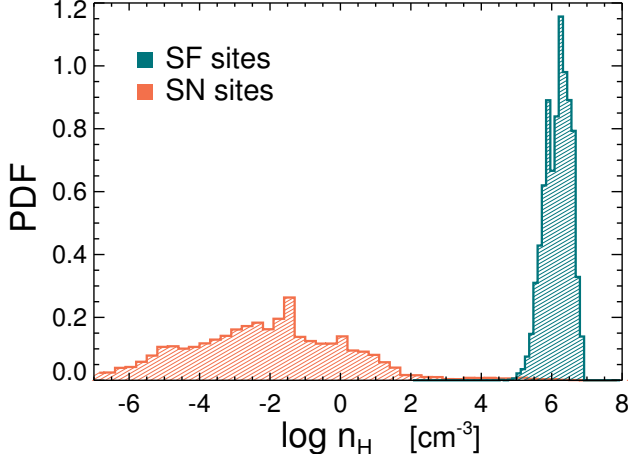


Figure 5. Local environments of star formation and Type II SN explosions in our mini-halo simulations. Even though stars form in very dense media, SN explosions occur in low-density regions. This is firstly because radiation lowers the ambient density before SN explosions, and secondly because the lifetime of massive stars ranges from 3 to 40 Myr and late explosions take advantage of the early SN events.

Pop III stars with $M_{\text{PopIII}} \lesssim 70 M_{\odot}$ is absorbed inside the virial radius.

The high escape fraction can be associated with the blow out of birth clouds due to radiation feedback (i.e. photoionisation plus direct radiation pressure). This is especially evident for Pop III stars, as they tend to form in an isolated fashion and radiation is the only energy source while they are emitting LyC photons. Even for Pop II star clusters, we find that radiation feedback is the main culprit for creating the low-density, ionised channels through which LyC photons can escape. This is supported by the short time delay ($\lesssim 5$ Myr) between the peak of the photon production rate and the peak of the escape fraction. Even though the youngest SN occurs after 3.5 Myr, the stochasticity in our random sampling of the lifetime of SN progenitors is unlikely to explain the short delay. To substantiate this further, we show an example in Figure 8 where the escape fraction increases from $f_{\text{esc}}(t_0) = 0\%$ to $f_{\text{esc}}(t_1) \sim 20\%$ within 3.7 Myr, during which no SN explosions occur. The dense, star-forming clouds are disrupted and LyC photons propagate to the virial radius, ionising the neutral hydrogen in the halo (second row). Note that only the birth clouds are dispersed, while the average density of the halo gas is little affected by radiation.

We find that SN explosions enhance the escape of LyC photons from time to time by ejecting gas from the dark matter halo. As an illustration, in Figure 8, we show the projected density distributions and the ionisation fraction of hydrogen at several different epochs. After the birth clouds are dispersed and lifted by radiation feedback ($t = t_1$), the density of the gas beyond the galaxy actually increases, obscuring the LyC photons in the halo region ($t = t_2$). Once this gas is completely pushed out from the halo, the column density of neutral hydrogen along these solid angles becomes very small ($t = t_3$, bottom middle panel). As a result, even though the projected ionised fraction at $t = t_3$ appears to be smaller than at the previous stage ($t = t_2$), the actual escape fraction is larger. Nevertheless, the effect of SNe by creating the secondary peak does not play a significant role in increasing the total number of escaping photons, as the stellar populations become too old to generate a large amount of LyC photons. It should be noted, however, that

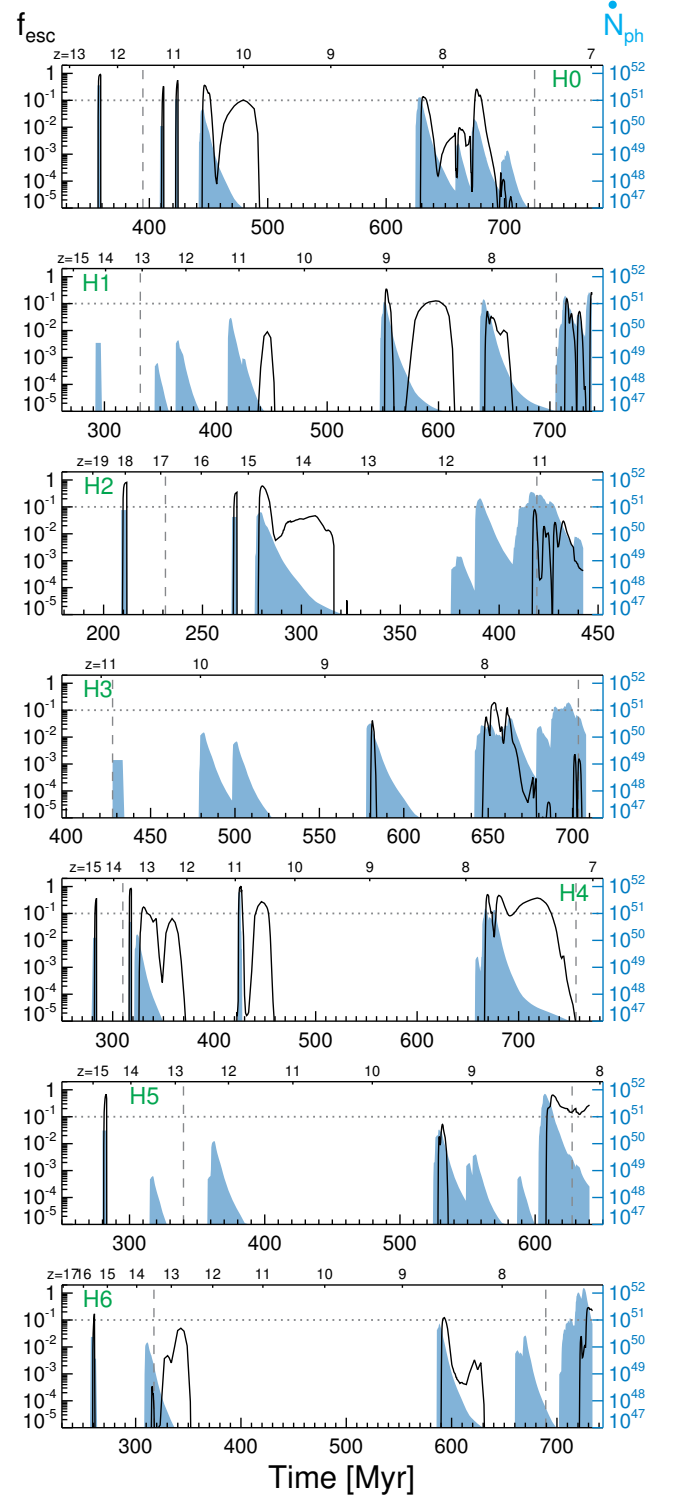


Figure 6. Evolution of the escape fraction (black lines) and the photon production rates (\dot{N}_{ph}) in units of $\# s^{-1}$ (cyan shaded regions) in seven different haloes as a function of the age of the Universe. The two vertical dashed lines mark the time at which the mass of each halo becomes 10^7 or $10^8 M_{\odot}$, respectively. The photons produced by Pop III and Pop II stars can be distinguished by the shape of the photon production rate; only Pop III stars exhibit a squarish evolution, because no LyC photons are generated once they explode or implode. Mini-haloes show a high escape fraction in general, although a significant variation can be seen. The escape fraction often exhibits a double peak for individual star formation events, which is explained in detail later in Figure 8.

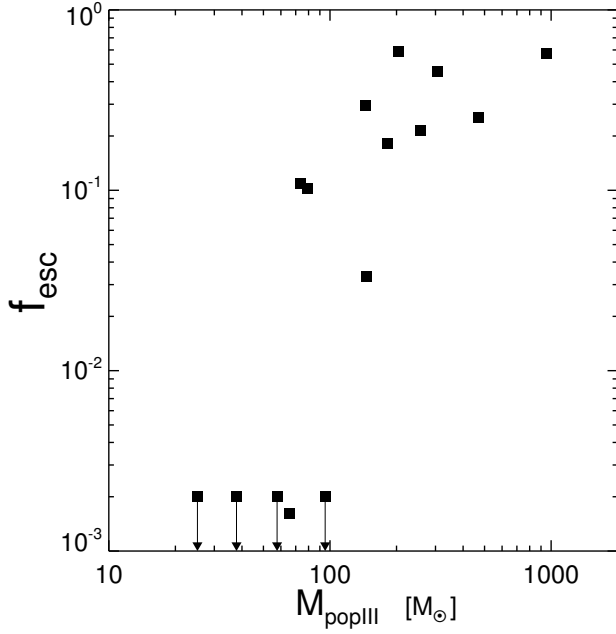


Figure 7. Escape fraction of individual Population III stars. We measure the mean escape fraction of Pop III stars by weighting the photon production rate during their lifetime. More massive Pop III stars show a higher escape fraction. We find that most LyC photons from low-mass Pop III stars ($M \lesssim 60 M_{\odot}$) are absorbed within the dark matter halo.

the effects of SNe may be more substantial if several star clusters form simultaneously in more massive haloes ($M_{\text{halo}} \gtrsim 10^8 M_{\odot}$) and SNe in slightly older clusters generate strong winds that strip off gas in other star-forming clumps (e.g., Kimm & Cen 2014).

In Figure 9, we show the average escape fraction as a function of the dark matter halo mass. As demonstrated in previous studies (Kimm & Cen 2014; Wise et al. 2014; Paardekooper et al. 2015), the instantaneous escape fraction varies significantly for a given halo mass. However, the photon-number weighted mean escape fraction in the mini-halo regime ($M_{\text{vir}} \leq 5 \times 10^7$) is found to be generally very high ($\sim 20\text{--}40\%$, Table 4). Note that this is a factor of a few larger than the average escape fraction predicted in atomic-cooling haloes ($f_{\text{esc}} \sim 10\%$, Kimm & Cen 2014), indicating that there is a dependence on the halo mass. It is also interesting to note that our results are in good agreement with Wise et al. (2014); Xu et al. (2016), despite the significant differences in the modelling of star formation and feedback. Nevertheless, both sets of studies (this work and Wise et al. (2014); Xu et al. (2016)) allow for rapid star formation which leads to the disruption of gas clumps. Wise et al. (2014) adopted 7% efficiency for star formation within a sphere of mean density $n_{\text{H}} \sim 10^3 \text{ cm}^{-3}$ per dynamical time, while our simulations employ an efficiency that varies ($\sim 5\text{--}20\%$) according to the local turbulent and gravitational conditions. The common prediction of the high f_{esc} suggests that there is a dominant feedback process, which is included in both studies, shaping the escape fraction in the mini-haloes. Indeed, as will be detailed later, we find that photoionisation is the main culprit for the effective leakage of LyC photons (see Section 4).

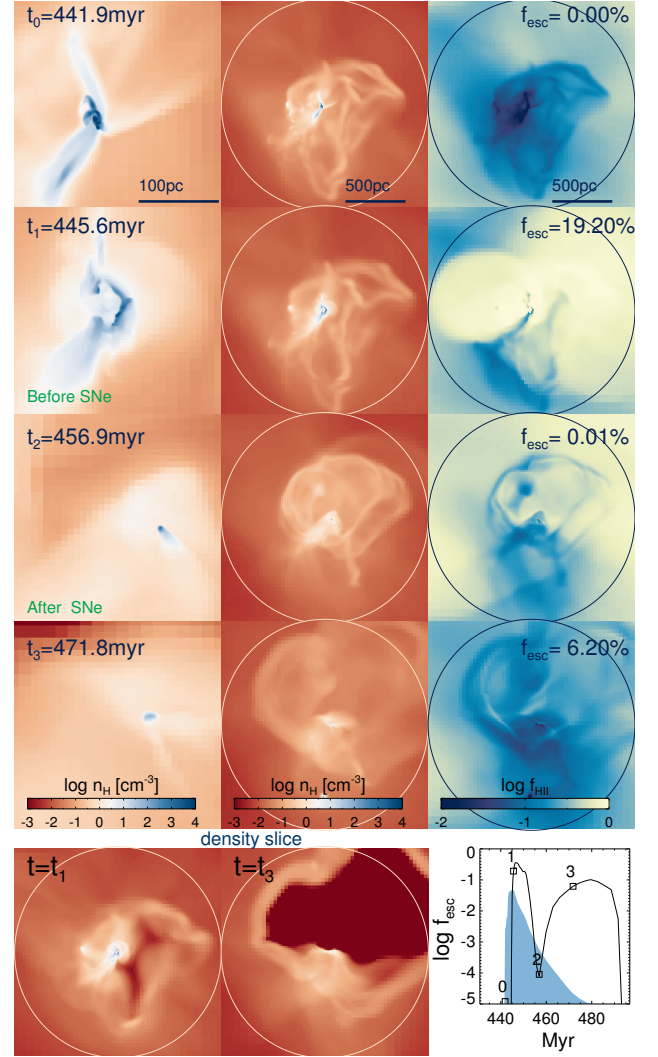


Figure 8. Origin of the double-peaked escape fraction for individual star formation events. The double-peaked feature is shown in the bottom right panel for clarity. The first column of the mosaic shows the evolution of the projected density distributions in the central region of the halo at four different times, as marked in the bottom right panel. The second and the third columns display the projected density and the fraction of ionised hydrogen distributions within a virial radius. The escape fraction at each time is also indicated in the top right corner. The bottom left panels show the density slice at two different epochs. One can see that the escape fraction becomes very high once the central star-forming clump is destroyed, and then drops as massive stars end their life. The escape fraction increases again when SNe blow out gas from the halo.

Table 4. Photon number-weighted f_{esc} at $7 \leq z \lesssim 15$

$\log M_{\text{vir}}$	$\langle f_{\text{esc}} \rangle$
6.40	$0.373^{+0.206}_{-0.350}$
6.83	$0.391^{+0.211}_{-0.339}$
7.07	$0.360^{+0.228}_{-0.219}$
7.49	$0.230^{+0.086}_{-0.074}$
7.95	$0.050^{+0.147}_{-0.026}$

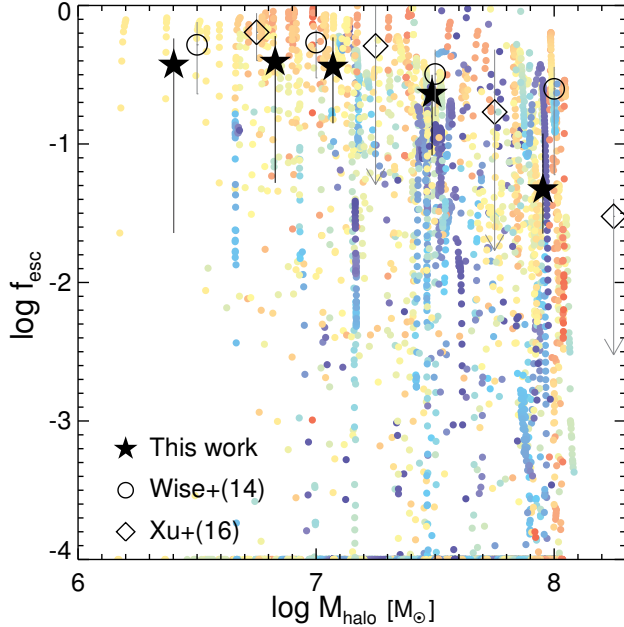


Figure 9. Escape fraction of LyC photons as a function of halo mass. Each point corresponds to the escape fraction in different haloes at various redshifts. Larger photon production rates are shown as redder colours. The photon number-weighted average is displayed as the star symbols with error bars representing the interquartile range (see Table 4). We find that the photon-weighted escape fraction is high ($\sim 20\text{--}40\%$) in the mini-haloes, in good agreement with the previous studies (Wise et al. 2014; Xu et al. 2016), even though there is a considerable scatter in instantaneous measurements.

3.2.2 Low Escape Fraction Due to Slow Destruction of Birth Clouds

Even though the leakage of LyC photons in the mini-haloes is very efficient on average, mini-haloes are sometimes optically thick for the LyC photons to escape (Figure 6). In order to understand the origin of the occasionally low escape fraction, we compute the optical depth centred on each young (< 10 Myr) star by casting 3072 rays per stellar particle using the HealPix algorithm (Górski et al. 2005). We adopt the absorption cross-section for neutral hydrogen from Osterbrock & Ferland (2006), and the Small Magellanic Cloud-type extinction curve for dust (Weingartner & Draine 2001) assuming that the dust mass constitutes 40% of the metal mass (e.g., Dwek 1998; Draine & Li 2007). We neglect the contribution from metals residing in hot gas with $T > 10^6$ K, as they are likely to be thermally sputtered (e.g., Draine & Salpeter 1979).

In Figure 10, we examine the minimum distance within which 50% and 99.9% of the LyC photons would be absorbed. Also included in the bottom panel is the local density at which each young star is located. Since we are interested in the origin of the low escape fraction even after a burst of star formation, we restrict our analysis to $11 < z < 13$ in H1, $11.2 < z < 12$ in H2, $9.5 < z < 10$, $7 < z < 7.5$ in H3, and $7.5 < z < 8$ in H6. The plot demonstrates that the escape fraction is low in two circumstances. First, a high density of the local environment ($n_H \gtrsim 10^3 \text{ M}_\odot$) indicates that stars are either just born out of dense clouds or radiation is not strong enough to blow away the surrounding medium. In this case the rays from these young star particles typically propagate to a small distance ($r \lesssim 10$ pc), implying that they get absorbed within the birth clouds. Such stars account for

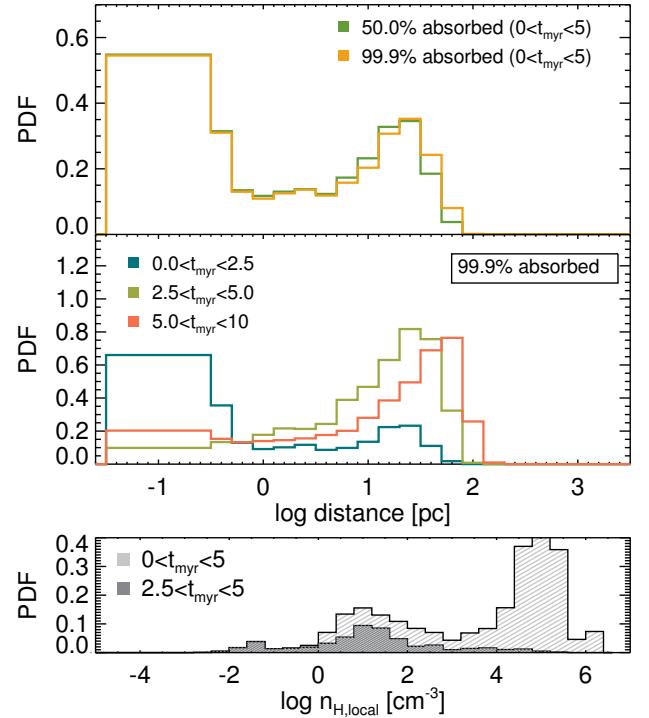


Figure 10. *Top panel:* probability distribution functions (PDFs) of the distance within which photons from stars younger than 10 Myr are absorbed when the escape fraction is low ($f_{\text{esc}} < 10^{-4}$) even after starbursts. These, for example, correspond to $11 < z < 11.5$ in H2 or $7 < z < 8$ in H6 (see text). Also included as a dark red line is the PDF of the distance within which 99.9% of the photons from stars of age $5 < t < 10$ Myr is absorbed. *Bottom panel:* probability distribution function of the local density at which the young stars are located.

$\sim 70\%$ of the low escape fraction. Second, stars with older ages ($t \gtrsim 2.5$ Myr) show progressively larger minimum distances (the middle panel), meaning that the birth clouds are dispersed at later stages. The trend that older stars are located in lower density environments supports this interpretation (the bottom panel). Once the dense structures are destroyed, photons propagate out to a larger radius ($r \gtrsim 10$ pc), but only a small fraction of the total ionising radiation appears to be able to do so. The similarity of the density PDFs for 50 % and 99.9 % absorption probability in the top panel suggests that the photon luminosity is sufficiently weak for the ionisation front to stall inside the halo. The composite image of H5 in Figure 2 illustrates an example of such a case. Thus, the escape fraction can sometimes be low even after a burst of star formation mainly because the birth clouds are cleared away too slowly compared to the lifetime of massive stars (~ 5 Myr).

4 DISCUSSION

4.1 Physical mechanism for driving the escape of LyC photons in mini-haloes

In the previous section, we showed that the high escape fraction is best explained by strong radiation feedback. This raises the question, which mechanism within this category is primarily responsible for regulating the escape fraction (i.e., photo-heating, direction radiation pressure from UV photons, or multiply scattered

IR photons)? Whether or not multiply scattered IR photons govern the dynamics of the ISM in our primordial galaxies can be tested by examining the trapping factor in the dense regions of the ISM. The typical density of the star-forming clouds of size ~ 10 pc is $\sim 10^5 \text{ cm}^{-3}$ in our simulations, and their metallicity ranges from $Z \sim 10^{-4} Z_{\odot}$ to $10^{-2} Z_{\odot}$. Assuming a dust opacity of $\kappa_{\text{sc}} \sim 5 (Z/Z_{\odot}) \text{ cm}^2 \text{ g}^{-1}$ (Semenov et al. 2003), IR photons in the star-forming clouds have a maximum optical depth of $\tau_{\text{d}} = \kappa_{\text{sc}} \Sigma_{\text{gas}} \lesssim 0.3$. Note that τ_{d} will be reduced further if the smaller scattering cross-section is considered at temperatures lower than ~ 100 K (Semenov et al. 2003). This indicates that the IR photons are not efficiently trapped inside the ISM, and that reprocessing gives a negligible momentum boost in the metal-poor, mini-haloes (c.f., the $\text{min}\rho_Q$ case in Bieri et al. 2016).

The effects of photo-heating and direct radiation pressure are difficult to disentangle, because they operate simultaneously. Nevertheless, it is possible to estimate the maximum extent within which each process can balance the external pressure in the ISM. Rosdahl & Teyssier (2015) show that if the ambient gas temperature (T_0) is significantly lower than that of the HII bubble ($T_{\text{ion}} \approx 2 \times 10^4$ K), the gas density inside the bubble can be lowered due to over-pressurization, and the extent to which ionising radiation can balance recombination becomes larger by a factor of $(T_{\text{ion}}/T_0)^{2/3}$. Thus, the gas can be pressure-supported within r_{PH} ,

$$r_{\text{PH}} \approx 26 \text{ pc} \left(\frac{m_{\text{star}}}{10^3 M_{\odot}} \right)^{1/3} \left(\frac{n_{\text{H},0}}{10^3 \text{ cm}^{-3}} \right)^{-2/3} \left(\frac{T_{\text{ion}}}{10^4 \text{ K}} \right)^{2/3} \left(\frac{T_0}{10^2 \text{ K}} \right)^{-2/3}, \quad (28)$$

where $n_{\text{H},0}$ is the density of the ambient medium. On the other hand, the absorption of ionising radiation directly imparts momentum which offsets the external pressure within r_{DP} ,

$$r_{\text{DP}} = \sqrt{\frac{L}{4\pi n_{\text{H},0} c k_B T_0}} \approx 6.4 \text{ pc} \left(\frac{m_{\text{star}}}{10^3 M_{\odot}} \right)^{1/2} \left(\frac{n_{\text{H},0}}{10^3 \text{ cm}^{-3}} \right)^{-1/2} \left(\frac{T_0}{10^2 \text{ K}} \right)^{-1/2}. \quad (29)$$

Here we use $L = 2 \times 10^{36} \text{ erg s}^{-1}$ per $1 M_{\odot}$, adequate for an SSP with age younger than 5 Myr. As pointed out Rosdahl & Teyssier (2015), the direct radiation pressure from a massive star cluster dominates over the pressure from the warm ionised gas only in a very dense medium, as $r_{\text{PH}}/r_{\text{DP}} \propto (L n_{\text{H},0})^{-1/6}$.

In Figure 11, we compare the two radii given by Equations (28) and (29). We take the external pressure as the mass-weighted pressure in the neighbouring 26 cells. This approach is, no doubt, a simplification, given that the immediate neighbours may already be ionised and cannot represent the cold surroundings. Nevertheless, this is justifiable because we are interested in the mostly neutral region where the impact of direct radiation pressure can be strong. The intensity of ionising radiation is calculated by combining the luminosity of each star residing in each cell. Note that we only consider cells with temperatures low enough to contain neutral hydrogen ($T \leq 2 \times 10^4$ K). Figure 11 suggests that photo-heating is primarily responsible for blowing gas away in the ISM at densities lower than $n_{\text{H}} \sim 10^4 \text{ cm}^{-3}$, whereas direct radiation pressure dominates over photo-heating at very high densities. It is worth noting that, at such high densities, pressure equilibrium due to direct radiation pressure is achieved on very short time scales (i.e. less than a Myr, see Figure 4 in Rosdahl & Teyssier 2015).

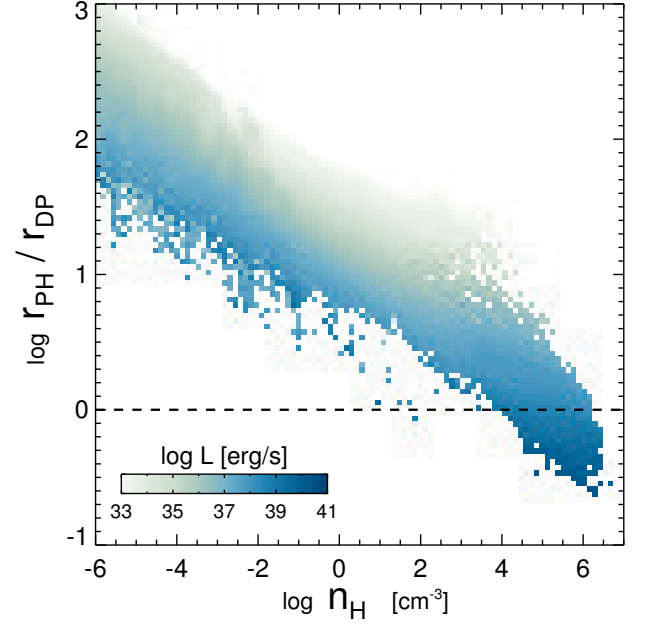


Figure 11. Comparison between the maximum radius within which photo-ionisation can counter-balance the external pressure (r_{PH}) and the radius within which direct radiation pressure can overcome the external pressure (r_{DP}). Only regions cooler than $T \leq 2 \times 10^4$ K are shown. Darker colours indicate the regions with stronger radiation field. The plot suggests that photo-ionisation is more important mechanism than direct radiation pressure in most regions, although direct pressure can be slightly more effective than photo-heating at emptying the gas in very dense regions.

Therefore, photo-heating is more likely to be responsible for the decrease in gas density than direct radiation pressure during the lifetime of massive stars (c.f., Haehnelt 1995).

To isolate the effects of photo-ionisation heating and radiation pressure, we identify a Pop III forming halo showing a high escape fraction ($f_{\text{esc}} \sim 10\%$) and run three simulations varying the included feedback processes. In the simulation without photo-heating (DP only), we compute the non-equilibrium chemistry without increasing the temperature by ionisation of hydrogen and helium. Figure 12 shows slices of density and ionised hydrogen fraction immediately preceding the explosion of a Pop III star with $M \approx 145 M_{\odot}$. It is evident from this figure that the efficient escape of LyC photons can be attributed to heating by photo-ionisation. The central star-forming cloud is effectively destroyed only in the runs with photo-heating.

Interestingly, we find that the run without photo-heating results in $f_{\text{esc}} = 0$, even though direct radiation pressure creates low-density holes in the central region of the dark matter halo. The density of the central hole is even lower than the run with photo-heating, because the UV photons accelerate the central gas more effectively due to lower temperature in the early stage of the expansion. Note that in order to receive a momentum boost from direct radiation pressure, atoms must be neutral and thus able to absorb ionizing radiation. Because UV photons from the Pop III star propagate and push the gas only in the radial direction, a dense shell structure that continually absorbs the ionising radiation is formed. This is an important difference from the run which includes photo-heating where the gas becomes over-pressurised and develops low-density channels naturally.

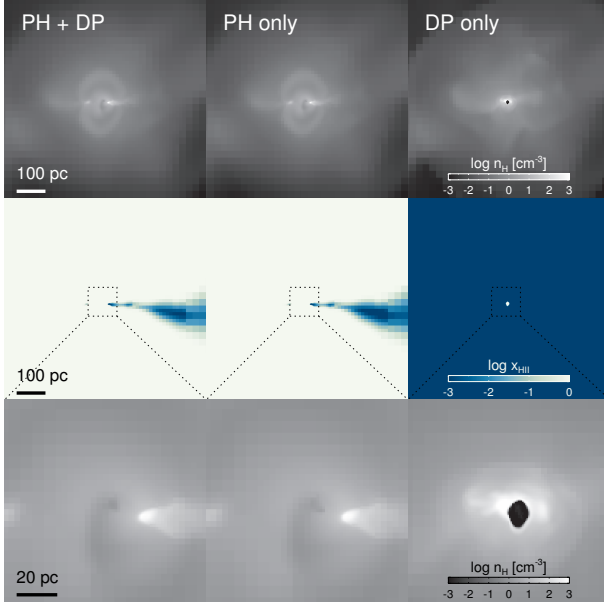


Figure 12. Effects of photo-heating (PH) and radiation pressure from UV photons (DP). The figure shows a slice of density (first and third rows) and ionised hydrogen fraction distributions (second row) from the simulations with and without PH and/or DP right after a Pop III star with $\approx 150 M_{\odot}$ is formed. The virial radius of the mini-halo is $R_{\text{vir}} \sim 350$ pc, which is approximately the size of the panels in the first and second rows. The panels in the third row are the zoomed-in images of the panels in the first row. It is evident that photo-heating is responsible for the efficient escape of LyC photons.

What, then, determines the escape fraction of LyC photons in the mini-haloes? Given the importance of photo-heating, the escape fraction is likely to depend on the strength of the radiation field. To investigate this issue, we measure the photon-number weighted escape fraction and the peak production rate of LyC photons for individual star formation episodes. Figure 13 (top panel) shows that the escape fraction is not strongly correlated with the peak production rate of LyC photons, indicating that it is not a simple function of star formation rate. However, taking the sample of Pop III stars alone, there is a trend that more massive stars show higher escape fractions, as seen in Figure 7. Given that the masses of their host dark matter haloes are more or less the same ($6.25 \lesssim \log M_{\text{halo}} \lesssim 7$), we hypothesise that the effect of photo-heating is likely to be mitigated if stars are enshrouded by a large amount of dense gas. To test this idea, we measure the gas mass for each solid angle assuming that a star cluster is a point source within the virial sphere. We exclude the gas less dense than n_{strom} , which is the maximum density below which recombination can be offset by the photons from Pop III or Pop II clusters. In addition, since photons in the outskirts of dense clouds are likely to escape more easily and LyC photons usually escape through a small opening angle with a low neutral fraction (e.g., Cen & Kimm 2015; Kim et al. 2013), we use the lowest 10% of the projected mass for each solid angle. Note that this is essentially the same as probing when the escape fraction is greater than 10%. The bottom panel of Figure 13 reveals that mini-haloes exhibit a high escape fraction when they form a lot of stars while there is a small amount of enshrouding gas. This is not particularly surprising and is also physically sensible because the more photons the halo has per dense gas mass, the more likely the ISM will be ionised and over-pressurised. One might wonder whether or not the

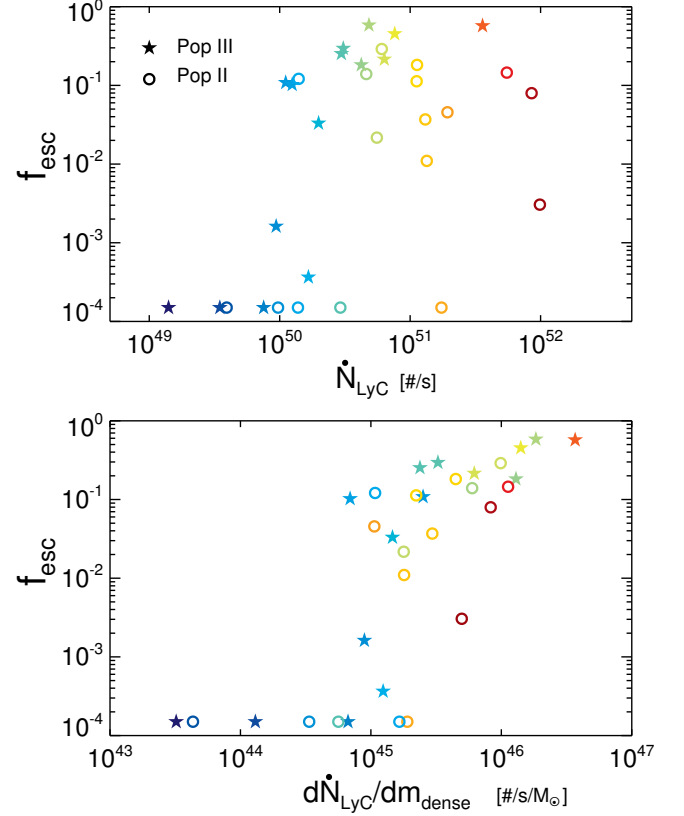


Figure 13. Origin of the high escape fraction. *Top panel* shows the photon-number weighted escape fraction of each star formation event as a function of the peak photon production rate (\dot{N}_{LyC}), which is essentially proportional to star formation rate. Each event involving Pop II and III stars is shown with different symbols, as indicated in the legend. Redder colours denote a larger \dot{N}_{LyC} . The escape fraction is weakly correlated with \dot{N}_{LyC} . *Bottom panel*: Same as the top panel, but with respect to the peak photon production rate per lowest 10% dense gas mass from each solid angle ($\frac{d\dot{N}_{\text{LyC}}}{d\Omega} / \frac{dm_{\text{dense}}}{d\Omega}$). Using the lowest 10% is motivated by the fact that LyC photons usually escape through a small opening angle with little neutral hydrogen. Here we define the dense gas as $n_{\text{H}} \geq n_{\text{H,strom}}$, where $n_{\text{H,strom}}$ is the minimum density below which gas can be fully ionised for a given \dot{N}_{LyC} . The escape fraction is higher if there are more photons available per dense gas mass. We interpret this as being mainly due to photoionisation feedback being more effective when there is less dense gas.

correlation arises simply due to the slim geometry of enshrouding gas. We confirm that taking the mean of the dense gas mass for each solid angle rather than the lowest 10% mass does not wash out the trend, but only weakens it slightly, suggesting that geometry is a secondary effect.

4.2 Importance of mini-haloes for reionisation

Our simulations represent only a small volume of the observable Universe, and thus it is not possible to calculate τ_e directly. Instead, we take a simple analytic approach to infer the importance of the mini-haloes to the reionisation history by computing the evolution of the mass fraction of ionised hydrogen (Q_{HII}), as

$$\frac{dQ_{\text{HII}}}{dt} = \frac{\dot{n}_{\text{ion}}}{\langle n_{\text{H}} \rangle} - \frac{Q_{\text{HII}}}{t_{\text{rec}}(C_{\text{HII}})}, \quad (30)$$

where $\langle n_H \rangle$ is the mean density of the universe in comoving scale. The recombination timescale (t_{rec}) is a function of a clumping factor (C_{HII}) and temperature, as

$$t_{\text{rec}}(C_{\text{HII}}) = [C_{\text{HII}} \alpha_B(T) f_e(z) \langle n_H \rangle (1+z)^3]^{-1} \quad (31)$$

where a correction factor ($f_e(z)$) is included to account for the additional contribution from singly ($z > 4$) or doubly ($z < 4$) ionised helium to the number density of electron (e.g., [Kuhlen & Faucher-Giguère 2012](#)). We adopt a redshift-dependent “effective” clumping factor of $C_{\text{HII}} = 1 + \exp(-0.28z + 3.59)$ at $z \geq 10$ or $C_{\text{HII}} = 3.2$ at $z < 10$ ([Pawlik et al. 2009](#)). Once Q_{HII} is determined, the Thomson optical depth is calculated as

$$\tau_e(z) = c \langle n_H \rangle \sigma_T \int_0^z f_e(z') Q_{\text{HII}}(z') \frac{(1+z')^2 dz'}{H(z')}. \quad (32)$$

The most crucial term in Equation (30) is the photon production rate per unit volume \dot{n}_{ion} ($\# \text{ Mpc}^{-3} \text{ s}^{-1}$). To compute this quantity, we first generate dark matter halo mass functions as a function of redshift ([Sheeth & Tormen 2002](#)), and assign stars to each dark matter halo by taking into account the following factors:

a) *Star formation efficiency*

[Kimm & Cen \(2014\)](#) performed cosmological radiation-hydrodynamic simulations, and showed that the UV luminosity function at $z \sim 7$ can be reproduced with efficient SN feedback. They find that the stellar mass to the dark matter halo mass may be approximated by the fit,

$$\log M_{\text{star}} = -8.08 + 1.55 \log M_{\text{halo}} \quad (33)$$

(see Figure 4, the black line). Our simulations suggest that the relation can be extended even to the mini-halo regime at $7 \lesssim z \lesssim 15$. Thus, we use this fit to compute the total stellar mass formed in each dark matter halo assuming no redshift dependence.

b) *Occupation fraction*

Not all of the mini-haloes hosts Pop II stars. This is essentially because early stars pre-heat the IGM and suppress the accretion on to the halo ([Gnedin 2000](#)). Moreover, the formation of molecular hydrogen, which is a prerequisite for gas collapse in mini-haloes in the absence of metals, is suppressed by the Lyman-Werner radiation from the neighbouring haloes. Furthermore, gas in haloes can be blown out by efficient feedback processes from Pop III stars. To account for the occupation fraction in haloes with $M_{\text{halo}} \geq 10^7 M_\odot$, we use a redshift-dependent fit to the fraction of haloes that host stars in the [Wise et al. \(2014\)](#) simulations (see their Figure 2). This corresponds to $f_{\text{host}} \approx 1$ for $M_{\text{halo}} \geq 10^7 M_\odot$ at $z \gtrsim 17$, while f_{host} drops to less than 0.01 in haloes with $10^7 M_\odot$ at $z \sim 7$. For haloes with $M_{\text{halo}} \leq 10^{6.25} M_\odot$ and $M_{\text{halo}} \geq 10^8 M_\odot$, we adopt a fixed value of $f_{\text{host}} = 2.4 \times 10^{-4}$ and unity, respectively ([Wise et al. 2014](#)). The occupation fraction is considered by simply reducing the number density of dark matter haloes that can form stars in estimating \dot{n}_{ion} (Equation 30).

c) *Escape fraction*

Our estimates of the escape fraction in mini-haloes are in good agreement with the results performed with ENZO ([Wise et al. 2014](#); [Xu et al. 2016](#)). However, the escape fractions in atomic-cooling haloes appears to be less certain, and thus we compare three different models: i) an escape fraction that slowly decreases with the halo mass ([Kimm & Cen 2014](#); [Xu et al. 2016](#)), ii) an escape fraction showing a more rapid decline (e.g., [Paardekooper et al. 2015](#); [Ma et al. 2015](#)), and iii) an escape fraction with a lower limit of 20%.

For the fiducial case, we employ the fit,

$$\log f_{\text{esc}} = 1.0 - 0.2 \log M_{\text{halo}}, \quad (34)$$

whereas a broken law is adopted for the “low” case

$$\log f_{\text{esc}} = \begin{cases} 0.17 - 0.2 \log M_{\text{halo}} & (M_{\text{halo}} > 10^{8.5}) \\ 9.52 - 1.3 \log M_{\text{halo}} & (10^{7.75} < M_{\text{halo}} \leq 10^{8.5}) \\ 1.0 - 0.2 \log M_{\text{halo}} & (M_{\text{halo}} \leq 10^{7.75}) \end{cases} \quad (35)$$

The last model has the same escape fraction as the fiducial case, but with the minimum of $f_{\text{esc}} = 20\%$, as is often assumed in reionisation studies. The three models are shown in Figure 14 (the top left panel). Also included as a dot-dashed line is a model with an escape fraction that would be necessary to yield a later end of reionisation as perhaps suggested by the Ly α opacity data presented by [Becker et al. \(2015\)](#).

$$\log f_{\text{esc}} = 1.292 - 0.245 \log M_{\text{halo}}, \quad (36)$$

d) *Metallicity-dependent \dot{N}_{ion}*

Metal-rich main sequence stars are cooler than metal-poor stars, and because of the larger opacity in the stellar atmosphere a SSP of solar metallicity produces approximately a factor of 2.5 fewer LyC photons than a SSP with $0.02 Z_\odot$. In order to not over-estimate the photon budget from metal-rich, massive galaxies, we take into consideration the metallicity-dependent \dot{N}_{ion} by using the local mass-metallicity relation for dwarf galaxies ([Woo et al. 2008](#)), as $\log Z = -3.7 + 0.4 \log (M_{\text{star}}/10^6 M_\odot)$. Although this is certainly a simplification that needs to be tested against upcoming high- z observations, we note that our simulated galaxies are metal-poor by about a factor of two compared to the relation, well within the scatter of the measurements. Once the metallicity of stars is determined, we use the metallicity-dependent number of LyC photons per M_\odot , as

$$\log Q_{\text{LyC}} = 60.31 - 0.237 \log Z, \quad (37)$$

which is appropriate for the Padova AGB models with a Kroupa IMF ([Leitherer et al. 1999](#)). Here we adopt a maximum mass cut-off of $120 M_\odot$ for the metallicity range $0.0004 \leq Z \leq 0.05$. We do not extrapolate Q_{LyC} for metallicities lower than $0.02 Z_\odot$. It is worth noting that for $Z = 0.004$, the Padova AGB model predicts $Q_{\text{LyC}} = 8.86 \times 10^{60}$, while the binary evolutionary model with a $300 M_\odot$ cut off gives a slightly higher estimate of $Q_{\text{LyC}} = 9.26 \times 10^{60}$ ([Stanway et al. 2016](#)). Stellar models with strong rotation seem to generate even more photons $Q_{\text{LyC}} = 11.2 \times 10^{60}$ at $Z = 0.002$ ([Topping & Shull 2015](#)), but this leads to only a minor increase ($\sim 20\%$) in the LyC production rate, which does not change our conclusions significantly.

e) *Pop III stars*

The largest uncertainty is perhaps the contribution of Pop III stars to reionisation. Not only is the IMF of the Pop III stars not well constrained, but also only a handful of Pop III stars are simulated in this work to estimate their escape fraction. Thus, we examine two extreme cases, one in which Pop III stars do not contribute to reionisation at all, and the other in which 40% of the photons from Pop III stars with $M_{\text{PopIII}} \gtrsim 100 M_\odot$ are assumed to contribute to reionisation. The former can be regarded as the case where only low-mass Pop III stars with $M_{\text{PopIII}} \lesssim 100 M_\odot$ form, whereas the latter corresponds to the case where one allows for the wide range

of masses from 10 to 1000 M_{\odot} . Note that the assumption of the mass-dependent escape fraction is motivated by Figure 7. The total number of LyC photons that Pop III stars can generate is computed by convolving the IMF (Equation 7) and the escape fraction. This yields $\langle N_{\text{LyC,PopIII}} \rangle = 1.8 \times 10^{62} M_{\odot}^{-1}$. We then adopt the formation rate of Pop III from the large volume simulations of Xu et al. (2016) (the “Normal” run) by using the fit, $\log \dot{M}_{\text{PopIII}} / (M_{\odot} \text{ yr}^{-1} \text{ Mpc}^{-3}) = -6.428 + 0.275 z - 0.011 z^2$. This rate is roughly an order of magnitude smaller than the rate employed in Wise et al. (2014), which is based on the simulation of an over-dense region (“Rare Peak”, H. Xu, priv. comm.).

Once the number of photons escaping from a dark matter halo ($N_{\text{LyC}}^{\text{esc}}$) as a function of M_{halo} and z is computed, the total number of escaped photons until z can be obtained by multiplying the dark matter halo mass function with $N_{\text{LyC}}^{\text{esc}}$. We use the Sheth & Tormen (2002) mass function for the mass range $M_{\text{halo}} = 10^{6.25} M_{\odot}$ to $10^{12} M_{\odot}$. The time derivative of the integrated quantity corresponds to \dot{n}_{ion} in Equation (30).

The top right panel in Figure 14 shows the evolution of \dot{n}_{ion} for the different models. In the cases with the fiducial escape fraction, the number of LyC photons that escape from their host halo peaks at $z \sim 5$ and decreases at lower redshift, in remarkably good agreement with the observational findings at $3 \leq z \leq 4.7$ (Becker & Bolton 2013). Note that the peak is earlier than the peak of the star formation rate density ($z \sim 3$, e.g. Hopkins & Beacom 2006), because the photon budget at $z \lesssim 6$ is determined by more massive, metal-enriched galaxies where fewer ionising photons are generated per mass of stars formed than in dwarf galaxies. The peak would shift to even earlier redshifts if the escape fraction decreases at lower redshifts. Although we assume a redshift-independent escape fraction, which is motivated by our simulations and simulations of Wise and collaborators at $z \gtrsim 7$, there is a hint that the escape fraction decreases with decreasing redshift. For example, from cosmological radiation-hydrodynamic simulations, Cen & Kimm (2015) measured that the escape fraction is decreased by a factor of ~ 2 at $z \sim 4$, compared to galaxies at $z \gtrsim 7$ (Kimm & Cen 2014). They attribute this to the fact that birth clouds are more slowly disrupted, as star formation becomes less stochastic at lower redshift. Thus, we caution the readers that \dot{n}_{ion} at $z \leq 6$ is probably still uncertain by a factor of a few. Our redshift-independent assumption should thus be kept in mind in our discussion of the reionisation history of the Universe at $z \gtrsim 6$.

Figure 14 depicts the evolution of the electron optical depth (τ_e), and the fraction of ionised gas (Q_{HII}). Several important conclusions can be drawn from this plot. First, the mini-haloes turn out to be of minor importance to reionisation. Although their escape fraction is high, the photon production rate is intrinsically low, firstly because stellar feedback efficiently suppress star formation, and secondly because not every mini-halo hosts stars (Gnedin 2000; Wise et al. 2014). We find that even if all the mini-haloes are assumed to host stars, τ_e will only increase slightly (model VI). Conversely, if we neglect the mini-haloes, there is no noticeable difference to the prediction of the reionisation history. This is in stark contrast with the claim that mini-haloes provide enough photons in the early universe to achieve a high $\tau_e \gtrsim 0.1$ (Wise et al. 2014). The difference can be attributed to a large part to the reduced stellar masses in the smallest mini-haloes in this work, compared to Wise et al. (2014).

Similarly, we find that the contribution from Pop III stars is not substantial (see also Paardekooper et al. 2013, c.f., Ahn et al. 2012; Maio et al. 2016). The model without Pop III stars (model

VI) predicts a minor decrease (35% and 10%) in the number of ionising photons at $z \sim 20$ and $z \sim 10$, respectively (see also Figure 15). The resulting difference in τ_e is found to be much smaller than the 1σ error of the Planck measurements. This strongly suggests that even if the characteristic mass of Pop III stars is lower ($\sim 40 M_{\odot}$), which prohibits them from ionising the IGM, the optical depth measurement may not be able to put strong constraints on the properties of Pop III stars (c.f., Visbal et al. 2015).

Instead, we find that the prediction of τ_e is primarily sensitive to the escape fraction of the atomic cooling haloes ($M_{\text{halo}} \gtrsim 10^8 M_{\odot}$). Our fiducial model with the relatively high escape fraction and Pop III stars yields $\tau_e \approx 0.067$, which is in reasonable agreement with the Planck measurements (Planck Collaboration et al. 2015, 2016). We also find that the evolution of Q_{HII} lies between that of the ‘Late’ and the ‘Very Late’ reionisation model of Choudhury et al. (2015) at $z \geq 8$ (see also Kulkarni et al. 2016), both of which are shown to be able to reproduce the rapid drop in the fraction of Ly α emitters at $z \gtrsim 7$ (Choudhury et al. 2015). On the contrary, the model with the “Low” escape fraction in the atomic-cooling regime fails to ionise the universe by $z \sim 3$ and under-predicts τ_e , even in the presence of the mini-haloes and Pop III stars. This demonstrates that massive stars in atomic-cooling haloes are likely to be the main sources responsible for reionising the Universe. In order for this “Low” escape fraction model to fully ionise the Universe by $z \sim 6$, a large number of AGN would be necessary at high redshifts to provide enough LyC photons (e.g., Madau & Haardt 2015). This scenario is certainly not yet ruled out, but it depends critically on the assumption about the evolution of the emissivity as a function of redshift, which is still a matter of debate (Giallongo et al. 2015; Kashikawa et al. 2015; Kim et al. 2015; Chardin et al. 2015).

When the escape fraction is assumed to always be greater than 20%, the optical depth is predicted by our models to be rather high ($\tau_e = 0.075$) and reionisation ends early ($z \sim 8$), which is less favoured by the latest Planck measurements ($\tau_e = 0.055 \pm 0.009$). Such a model also struggles to explain the evolution of the Ly α opacity (fluctuations) in QSO spectra at $z > 5$ as well as the rapid evolution of Ly α emitters (Becker et al. 2015; Chardin et al. 2015; Choudhury et al. 2015). In fact, even our fiducial model predicts reionisation at $z \sim 6.7$, slightly earlier than in the fiducial model of Chardin et al. (2015) that fits well the photo-ionisation rate inferred from Ly α forest data and perhaps suggesting that the escape of LyC photons in the atomic-cooling haloes needs to be suppressed further.

It should be noted, however, that there is a possibility that the simple analytic calculations are likely to predict too rapid propagation of HII bubbles in the late stage of reionisation ($z \lesssim 8$) due to the assumption of infinite speed of light used in Equation (30). In practice, photons from massive haloes will have to travel to encounter neutral hydrogen in regions devoid of sources, which inevitably delays the propagation of HII bubbles. If this is the case, reionisation in the fiducial model is likely to end later than $z = 6.7$, bringing the optical depth in better agreement with the latest Planck results. However, the precise determination of the delay requires large-scale reionisation simulations that are calibrated to match the photon production rates from haloes of different masses in this study, hence it is not clear yet how significant the effect will be. If the propagation of HII bubbles is not significantly overestimated in our simple calculations, the escape fraction needs to be reduced further in more massive haloes in order for dwarf galaxies to reionise the universe only by $z \leq 6$, as in our “Late z_{reion} ” model shown by the dot-dashed line in Figure 14. Such escape fractions in atomic-

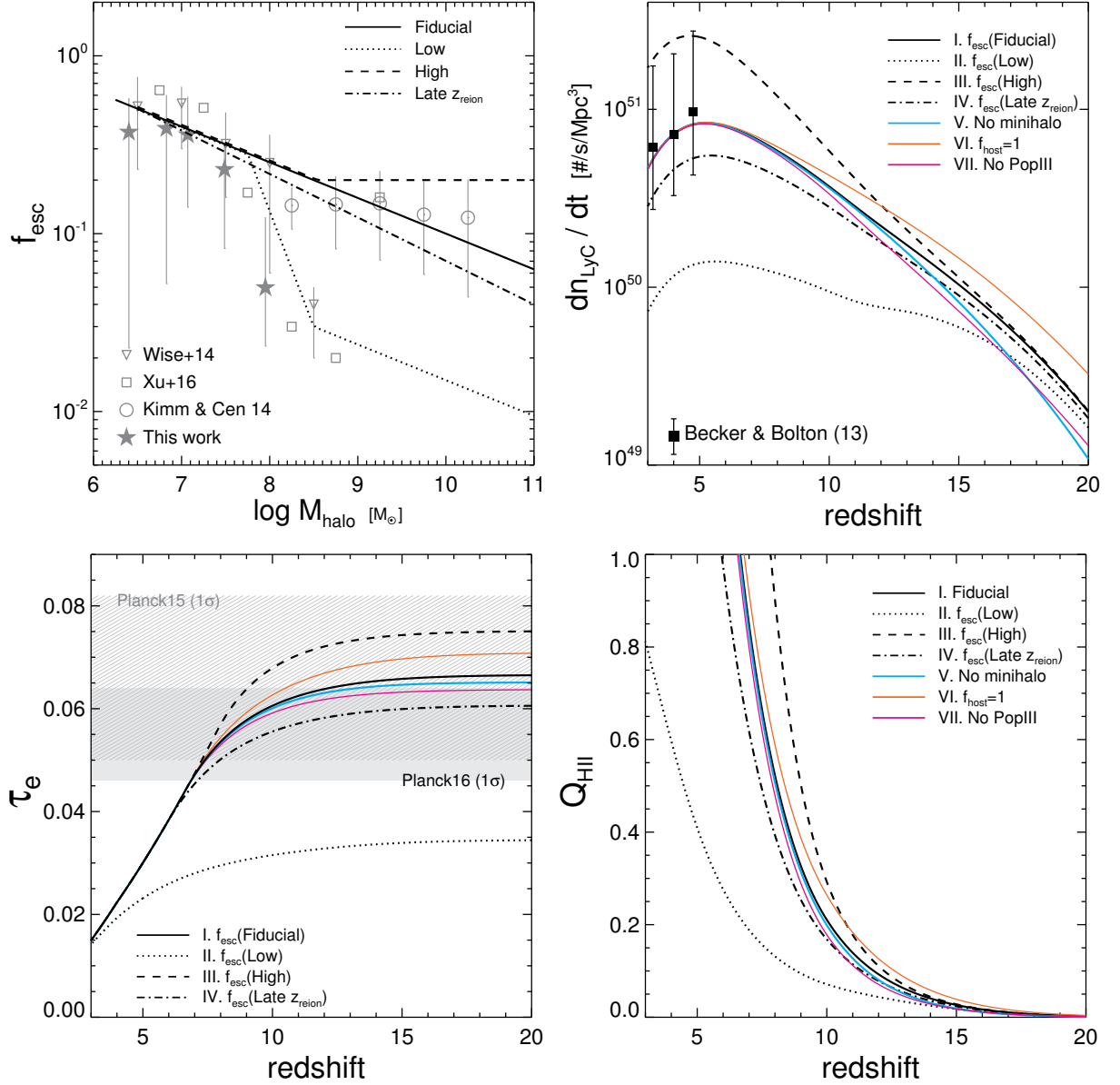


Figure 14. Reionisation models based on simple analytic calculations. We examine three different escape fractions (models I, II, and III), the presence of the mini-haloes (model V) or Pop III stars (model VII), and the occupation fraction of the mini-haloes (model VI). Also included as model IV is the escape fraction favoured by the patchy reionisation picture (Becker et al. 2015). *Top left:* different assumptions about the escape fraction used to calculate the reionisation history. Different symbols indicate the escape fraction from different theoretical studies, as indicated in the legend. The solid, dashed, and dotted line represent the fiducial, high, and low escape fraction model, respectively. *Top right:* The photon production rate per unit volume (dn_{LyC}/dt) as a function of redshift. We use the Sheth & Tormen (2002) mass functions and our theoretical results (the dashed line in Figure 4, Equation 33) to compute dn_{LyC}/dt . *Bottom left:* The electron optical depth (τ_e) in different models. The optical depths inferred from the Planck experiments are shown as shaded regions (light grey: Planck Collaboration et al. 2015, dark grey: Planck Collaboration et al. 2016). *Bottom right:* The fraction of ionised hydrogen. Our fiducial model predicts the reionisation redshift of 6.7 and $\tau_e = 0.067$. We find that the mini-haloes produce a rather small amount of LyC photons, and thus are of minor importance for the reionisation of the Universe.

cooling haloes are certainly within the uncertainty of current numerical results, and it would be worthwhile to re-examine escape fractions in more massive haloes ($M_{\text{halo}} \geq 10^{10} M_{\odot}$) with the physically well-motivated thermo-turbulent star formation model employed here where stars form preferentially in gravitationally bound regions, and see how it compares with the results based on a simple density criterion for star formation (Kimm & Cen 2014).

In the left panel of Figure 15, we show the relative contribution of LyC photons from different components for our fiducial

reionisation model. It can be seen that more massive haloes dominate the photon budget at lower redshift in this model, and that reionisation is driven by intermediate-mass atomic cooling haloes ($10^8 M_{\odot} \lesssim M_{\text{halo}} \lesssim 10^{11} M_{\odot}$). The current theoretical estimate of Pop III star formation rates (Xu et al. 2016) suggests that Pop III stars are important only at $z \gtrsim 15$. The plot also demonstrates that the photon production rate density decreases at $z \lesssim 5$ in our model, essentially because the number density of the intermediate-mass haloes with $10^8 M_{\odot} \lesssim M_{\text{halo}} \lesssim 10^{11} M_{\odot}$ does not increase any-

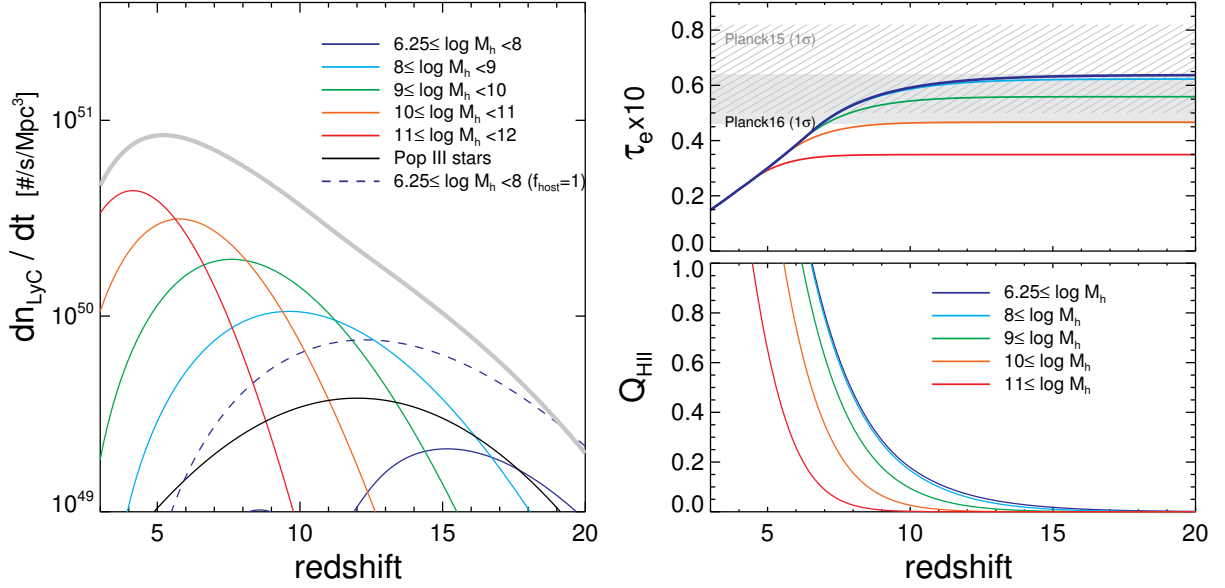


Figure 15. *Left:* Contribution of photons from different halo masses to reionisation as a function of redshift. We adopt the fiducial model for escape fractions (the black solid line in Figure 14) and the stellar mass-to-halo mass relation from this work (the dashed line in Figure 4). The photon production rate density from Pop III stars is shown as the black dashed line. The dotted line displays the maximum contribution from mini-haloes assuming that all of them host stars ($f_{\text{host}} = 1$). *Right:* The electron optical depth (top) and the fraction of ionised hydrogen (bottom) for models with different minimum halo masses, as indicated in the legend. The plots demonstrate that it is necessary to resolve haloes of mass $\approx 10^8 M_\odot$ to model reionisation in simulations.

more at lower redshift. One may wonder here whether the inclusion of more massive haloes with masses $M_{\text{halo}} \gtrsim 10^{12} M_\odot$ would change our conclusions, but we find that the photon production rate density from these haloes is significantly smaller than that from $M_{\text{halo}} \geq 10^{11} M_\odot$ at $z \gtrsim 3$ if the local $M_{\text{star}}-M_{\text{halo}}$ relation (Behroozi et al. 2013) is assumed, as star formation becomes less efficient in haloes with $M_{\text{halo}} \geq 10^{12} M_\odot$.

Our results indicate that it will be necessary to resolve haloes of mass $\approx 10^8 M_\odot$ in order to correctly capture the expansion of ionised HII bubbles in large-scale simulations. The right panels of Figure 15 show that neglecting the contribution of LyC photons from haloes less massive than $10^9 M_\odot$ will only marginally delay the expansion, reasonably reproducing the electron optical depth. However, simulations that cannot resolve haloes with $M_{\text{halo}} \lesssim 10^{10} M_\odot$ would need to adopt higher escape fractions than the values derived in this work to provide photons early enough (e.g., Ocvirk et al. 2015; Gnedin & Kaurov 2014; Pawlik et al. 2015).

4.3 Caveats

Even though we include the most important physical ingredients in our simulations, it should be mentioned that several potential issues which can affect the predictions of star formation and the escape fraction are neglected.

First, we do not take into account the fact that the mass of the most massive star within a cluster is correlated with the total cluster mass (Weidner et al. 2010; Kirk & Myers 2011). Given that the most massive stars are the most efficient at producing LyC photons, the number of photons per unit stellar mass (i.e. specific number) is likely to be over-estimated in the simulated small Pop II clusters of mass $M \leq 10^4 M_\odot$ where the IMF would not be fully sampled (see Kroupa et al. 2013, for a review). For example, at $Z = 0.0004$, the specific number of LyC photons from a

$10^3 M_\odot$ cluster is smaller by $\sim 60\%$ than that from a $10^4 M_\odot$ cluster. Neglecting this IMF sampling issue may have suppressed star formation more effectively than it should have. However, we do not expect that the escape fraction would be affected significantly by lowering N_{LyC} by a factor of two, given that the number of Ly α photons per dense gas mass spans three orders of magnitude already (Figure 13). Furthermore, it should be noted that the grids of the stellar tracks do not extend to values lower than $0.02 Z_\odot$. For comparison, star particles with $M < 10^4 M_\odot$ in our simulations often have the metallicity of $10^{-4}-10^{-3} Z_\odot$. We use the lowest grid point in order to not extrapolate the number of photons produced, but the use of more appropriate stellar grids is likely to enhance the Ly α photon production, possibly compensating the over-estimation due to the incomplete IMF sampling.

Second, we neglect the contribution from runaway stars, which are thought to form through three-body interactions within clusters (e.g., Gies & Bolton 1986; Leonard & Duncan 1988; Fujii & Portegies Zwart 2011) and/or the ejection in a binary system after the explosion of the primary star (e.g., Blaauw 1961; Portegies Zwart 2000). Using an analytic model of disc galaxies, Conroy & Kratter (2012) claim that the inclusion of the runaway stars can in principle enhance the escape fraction by up to an order of magnitude if f_{esc} without them is very small. However, Kimm & Cen (2014) compare the radiation-hydrodynamic simulations with and without the runaways, and show that the increase in f_{esc} due to runaways is small ($\sim 20\%$ level) mainly because f_{esc} is already high ($f_{\text{esc}} \sim 10\%$). In the same context, we do not expect that the runaways significantly affect the prediction of f_{esc} in mini-haloes where f_{esc} is even higher ($\sim 20-40\%$).

Third, our predictions are subject to the stellar evolutionary models. We take the production rate of LyC photons from the Padova model (Girardi et al. 2000; Leitherer et al. 1999), which is based on the evolution of single stars without rotation. However, it is known that many, if not all, massive stars live in binaries (e.g.,

Sana et al. 2012), and that their spin is non-negligible. The interactions of binary stars can not only increase the total number of LyC photons, but also make the decline of the production rate slower, as the primary star transfers gas to the secondary, removes the hydrogen envelope, and the stars merge (Stanway et al. 2016). Rotation can also increase the total number of ionising photons and the lifetime of massive stars by regulating the mixing and fuelling of gas into the stellar core (e.g., Ekström et al. 2012). As aforementioned, the adoption of the recent stellar models can increase the production rate of LyC photons by $\sim 10 - 20\%$ for an SSP (Topping & Shull 2015; Stanway et al. 2016), and is therefore not very important for the total photon production. However, these effects can potentially increase the escape fraction to the level of $\sim 20\%$ in galaxies hosted by massive haloes with $10^{10} - 10^{11} M_{\odot}$ (Ma et al. 2016), as stars older than $t \gtrsim 3$ Myr produce a non-negligible fraction of LyC photons. This could potentially bring the results of the simulations in tension with the rather late end of reionisation suggested by the CMB data as well as Ly α forest and Ly α emitter data, as dwarf galaxies would produce too many photons (see Figure 14). Future radiation-hydrodynamic simulations with the self-consistent modelling of binary populations are necessary to better understand the role of (massive) binary stars and to see if theory and observations can still be reconciled.

Finally, due to the limited computational resources we had available, the work presented here lacks the systematic investigation of the effects of numerical resolution on the prediction of the escape of LyC photons. However, we note that our resolution and refinement strategy allows for star formation in sufficiently dense and gravitationally bound regions, which should be essential to not over-estimate the escape fraction (e.g., Ma et al. 2015). Nevertheless, in order to make sure that this is really the case, we perform a resolution test by re-running the H1 halo with one fewer level of refinement (i.e. 1.4 pc resolution). We find that the escape fraction in the mini-halo is still high ($f_{\text{esc}} \sim 40\%$), although the stellar mass is increased by 30%. We also note that the recent work by Xu et al. (2016) shows that their 19 pc (comoving) resolution simulations (~ 2 pc, physical) yield the results consistent with their previous simulations with a higher resolution of 1 pc (comoving) (Wise et al. 2014). This suggests that the prediction of the escape fraction and star formation rates is likely to be converged in (sub-)parsec-scale simulations, as the physics of the collapse and subsequent disruption of star-forming clouds is reasonably well captured.

5 CONCLUSIONS

Using the radiation-hydrodynamic simulation code, RAMSES-RT, we investigate the importance of mini-haloes with $10^{6.25} \lesssim M_{\text{halo}} \lesssim 10^8 M_{\odot}$ for the reionisation history of the Universe. For this purpose, we run nine zoom-in, cosmological simulations with non-equilibrium photo-chemistry involving molecular hydrogen, star formation based on the local conditions of the ISM (i.e. thermo-turbulent model), radiation pressure from UV and IR photons, heating by photo-ionisation, and mechanical SN feedback. We measure the stellar mass and escape fractions from the simulations at $7 \leq z < 18$, and examine the relative importance of mini-haloes for reionisation by computing the evolution of the fraction of ionised hydrogen based on a simple analytic model. Our conclusions can be summarised as follows.

(i) We find that even though the instantaneous escape fraction is highly variable, the photon-number weighted average escape fraction is generally high ($\sim 20 - 40\%$) in mini-haloes (Figure 9),

in agreement with previous studies (Wise et al. 2014; Xu et al. 2016). The escape fraction is nevertheless occasionally low even after a burst of star formation, and we attribute this to the fact that in this case the disruption of the birth clouds is too slow for LyC photons to escape efficiently (Figure 10).

(ii) The process primarily responsible for the efficient escape of LyC photons in mini-haloes is heating due to photoionisation (Figure 11). Direct radiation pressure alone seems unlikely to create low-density channels through which ionising radiation can escape. Rather, it simply compresses gas radially, resulting in dense neutral gas shells (Figure 12). Because star formation is very stochastic with our thermo-turbulent model, strong radiation from young stars plays a significant role before SN explosions come into play. This leads to a short time-delay of $\lesssim 5$ Myr between the peak of the production rate of LyC photons and the escape fraction when ionising radiation can efficiently escape into the IGM (Figures 6 and 8).

(iii) Only massive Pop III stars ($M_{\text{PopIII}} \gtrsim 100 M_{\odot}$) can play a role in ionising the neutral gas beyond the virial radius. LyC photons from Pop III stars with lower masses ($M_{\text{PopIII}} \lesssim 70 M_{\odot}$) are mostly absorbed in the central region of their host halo (Figure 7).

(iv) The escape fraction for individual star formation events is not strongly correlated with the star formation rate (Figure 13). Instead, we find the the production rate of ionising photons per dense gas mass is the key to determining the escape fraction. Mini-haloes producing a large number of LyC photons per dense gas mass show a higher escape fraction. This also explains why the escape of LyC photons is significant in Pop III stars with $M_{\text{PopIII}} \gtrsim 100 M_{\odot}$.

(v) Star formation is efficiently regulated by feedback processes in the mini-haloes. The typical stellar mass in the mini-halo ranges from $10^3 -$ a few times $10^4 M_{\odot}$, meaning that only less than a few percent of baryons is converted into stars (Figure 4). Our simulated galaxies follow the normalisation and slope of the $M_{\text{star}} - M_{\text{halo}}$ sequence obtained from the radiation-hydrodynamic simulations by Kimm & Cen (2014), which is interestingly similar to the $z \sim 0$ empirical sequence by Behroozi et al. (2013) when extrapolated to the mini-halo regime.

(vi) Using a simple analytic approach, we find that the main driver of reionisation is the LyC photons from atomic-cooling haloes ($10^8 M_{\odot} \lesssim M_{\text{halo}} \lesssim 10^{11} M_{\odot}$). Although mini-haloes are more abundant and their escape fraction is higher than that of the more massive haloes, their contribution to reionisation is of minor importance, essentially because star formation is inefficient (Figure 14). Even if 100% of the mini-haloes are assumed to host stars, this does not alter our conclusions. Our fiducial model with a reasonably high escape fraction in the atomic-cooling regime predicts that the universe is fully ionised by $z \sim 6.7$ and $\tau_e = 0.067$. Although the optical depth estimation is consistent with the latest Planck measurement within the two sigma uncertainty, reionisation is predicted to end relatively early, which may be in tension with the rather late end of reionization suggested by the most recent CMB data as well as the Ly α forest and Ly α emitter data. A larger escape of $\sim 20\%$ in massive haloes with $10^9 - 10^{11} M_{\odot}$ would further raise this tension. Further investigation of the escape fraction in atomic-cooling haloes should shed light on this potential over-production of LyC photons.

ACKNOWLEDGEMENTS

We thank the anonymous referee for helpful comments that improved the manuscript. We are grateful to John Wise and Renyue Cen for helpful conversations and Romain Teyssier for making his code RAMSES publicly available. We also thank John Wise and Hao Xu for sharing the occupation fraction and the Pop III star formation rate data with us. This work was supported by the ERC Advanced Grant 320596 “The Emergence of Structure during the Epoch of Reionization” and the Spin(e) grants ANR-13-BS05-0005 of the French Agence Nationale de la Recherche (<http://cosmicorigin.org>). HK is supported by Foundation Boustany, the Isaac Newton Studentship, and the Cambridge Overseas Trust. JR was funded by the European Research Council under the European Unions Seventh Framework Programme (FP7/2007-2013)/ERC Grant agreement 278594-GasAroundGalaxies, and the Marie Curie Training Network CosmoComp (PITN-GA-2009-238356). JD and AS’s research is supported by funding from Adrian Beecroft, the Oxford Martin School and the STFC. This work used the DiRAC Complexity system, operated by the University of Leicester IT Services, which forms part of the STFC DiRAC HPC Facility (www.dirac.ac.uk). This equipment is funded by BIS National E-Infrastructure capital grant ST/K000373/1 and STFC DiRAC Operations grant ST/K0003259/1. DiRAC is part of the National E-Infrastructure.

REFERENCES

- Abel T., Bryan G. L., Norman M. L., 2002, *Science*, **295**, 93
- Ahn K., Iliev I. T., Shapiro P. R., Mellema G., Koda J., Mao Y., 2012, *ApJ*, **756**, L16
- Anninos P., Zhang Y., Abel T., Norman M. L., 1997, *New Astron.*, **2**, 209
- Aubert D., Teyssier R., 2008, *MNRAS*, **387**, 295
- Aubert D., Pichon C., Colombi S., 2004, *MNRAS*, **352**, 376
- Baczynski C., Glover S. C. O., Klessen R. S., 2015, *MNRAS*, **454**, 380
- Bakes E. L. O., Tielens A. G. G. M., 1994, *ApJ*, **427**, 822
- Becker G. D., Bolton J. S., 2013, *MNRAS*, **436**, 1023
- Becker R. H., et al., 2001, *AJ*, **122**, 2850
- Becker G. D., Bolton J. S., Madau P., Pettini M., Ryan-Weber E. V., Venemans B. P., 2015, *MNRAS*, **447**, 3402
- Behroozi P. S., Wechsler R. H., Conroy C., 2013, *ApJ*, **770**, 57
- Bieri R., Dubois Y., Rosdahl J., Wagner A. Y., Silk J., Mamon G. A., 2016, preprint, ([arXiv:1606.06281](https://arxiv.org/abs/1606.06281))
- Blaauw A., 1961, *Bull. Astron. Inst. Netherlands*, **15**, 265
- Blondin J. M., Wright E. B., Borkowski K. J., Reynolds S. P., 1998, *ApJ*, **500**, 342
- Bolton J. S., Haehnelt M. G., 2007, *MNRAS*, **382**, 325
- Bonazzola S., Heyvaerts J., Falgarone E., Perault M., Puget J. L., 1987, *A&A*, **172**, 293
- Borthakur S., Heckman T. M., Leitherer C., Overzier R. A., 2014, *Science*, **346**, 216
- Boutsia K., et al., 2011, *ApJ*, **736**, 41
- Bouwens R. J., et al., 2012, *ApJ*, **752**, L5
- Bridge C. R., et al., 2010, *ApJ*, **720**, 465
- Brodie J. P., Romanowsky A. J., Strader J., Forbes D. A., 2011, *AJ*, **142**, 199
- Bromm V., Coppi P. S., Larson R. B., 2002, *ApJ*, **564**, 23
- Bruzual G., Charlot S., 2003, *MNRAS*, **344**, 1000
- Bryan G. L., Norman M. L., 1998, *ApJ*, **495**, 80
- Bunker A. J., et al., 2010, *MNRAS*, **409**, 855
- Caruana J., Bunker A. J., Wilkins S. M., Stanway E. R., Lorenzoni S., Jarvis M. J., Ebert H., 2014, *MNRAS*, **443**, 2831
- Cen R., 2016, preprint, ([arXiv:1604.01986](https://arxiv.org/abs/1604.01986))
- Cen R., Kimm T., 2015, *ApJ*, **801**, L25
- Chardin J., Haehnelt M. G., Aubert D., Puchwein E., 2015, *MNRAS*, **453**, 2943
- Choudhury T. R., Puchwein E., Haehnelt M. G., Bolton J. S., 2015, *MNRAS*, **452**, 261
- Conroy C., Kratter K. M., 2012, *ApJ*, **755**, 123
- Couchman H. M. P., Rees M. J., 1986, *MNRAS*, **221**, 53
- Cowie L. L., Barger A. J., Trouille L., 2009, *ApJ*, **692**, 1476
- Dale J. E., Ngoumou J., Ercolano B., Bonnell I. A., 2014, *MNRAS*, **442**, 694
- Davies F. B., Furlanetto S. R., 2016, *MNRAS*, **460**, 1328
- Dopita M. A., Krauss L. M., Sutherland R. S., Kobayashi C., Lineweaver C. H., 2011, *Ap&SS*, **335**, 345
- Draine B. T., Li A., 2007, *ApJ*, **657**, 810
- Draine B. T., Salpeter E. E., 1979, *ApJ*, **231**, 77
- Draine B. T., et al., 2007, *ApJ*, **663**, 866
- Dwek E., 1998, *ApJ*, **501**, 643
- Ekström S., et al., 2012, *A&A*, **537**, A146
- Fan X., et al., 2001, *AJ*, **122**, 2833
- Fan X., et al., 2006, *AJ*, **132**, 117
- Federrath C., Klessen R. S., 2012, *ApJ*, **761**, 156
- Federrath C., Sur S., Schleicher D. R. G., Banerjee R., Klessen R. S., 2011, *ApJ*, **731**, 62
- Ferland G. J., Korista K. T., Verner D. A., Ferguson J. W., Kingdon J. B., Verner E. M., 1998, *PASP*, **110**, 761
- Finkelstein S. L., Papovich C., Giavalisco M., Reddy N. A., Ferguson H. C., Koekemoer A. M., Dickinson M., 2010, *ApJ*, **719**, 1250
- Finlator K., Oh S. P., Özel F., Davé R., 2012, *MNRAS*, **427**, 2464
- Fisher D. B., et al., 2014, *Nature*, **505**, 186
- Fontanot F., Cristiani S., Pfrommer C., Cupani G., Vanzella E., 2014, *MNRAS*, **448**, 3248
- Fujii M. S., Portegies Zwart S., 2011, *Science*, **334**, 1380
- Geen S., Rosdahl J., Blaizot J., Devriendt J., Slyz A., 2015, *MNRAS*, **448**, 3248
- Giallongo E., et al., 2015, *A&A*, **578**, A83
- Gies D. R., Bolton C. T., 1986, *ApJS*, **61**, 419
- Girardi L., Bressan A., Bertelli G., Chiosi C., 2000, *A&AS*, **141**, 371
- Glover S. C. O., Federrath C., Mac Low M.-M., Klessen R. S., 2010, *MNRAS*, **404**, 2
- Gnedin N. Y., 2000, *ApJ*, **535**, 530
- Gnedin N. Y., Kaurov A. A., 2014, *ApJ*, **793**, 30
- Gnedin N. Y., Kravtsov A. V., Chen H.-W., 2008, *ApJ*, **672**, 765
- Górski K. M., Hivon E., Banday A. J., Wandelt B. D., Hansen F. K., Reinecke M., Bartelmann M., 2005, *ApJ*, **622**, 759
- Grazian A., et al., 2016, *A&A*, **585**, A48
- Greif T. H., Glover S. C. O., Bromm V., Klessen R. S., 2010, *ApJ*, **716**, 510
- Greif T. H., Bromm V., Clark P. C., Glover S. C. O., Smith R. J., Klessen R. S., Yoshida N., Springel V., 2012, *MNRAS*, **424**, 399
- Guillet T., Teyssier R., 2011, *Journal of Computational Physics*, **230**, 4756
- Haardt F., Madau P., 2012, *ApJ*, **746**, 125
- Habing H. J., 1968, *Bull. Astron. Inst. Netherlands*, **19**, 421
- Haehnelt M. G., 1995, *MNRAS*, **273**, 249
- Haehnelt M. G., Madau P., Kudritzki R., Haardt F., 2001, *ApJ*, **549**, L151
- Hahn O., Abel T., 2011, *MNRAS*, **415**, 2101
- Haiman Z., Loeb A., 1998, *ApJ*, **503**, 505
- Halle A., Combes F., 2013, *A&A*, **559**, A55
- Heger A., Woosley S. E., 2002, *ApJ*, **567**, 532
- Heger A., Fryer C. L., Woosley S. E., Langer N., Hartmann D. H., 2003, *ApJ*, **591**, 288
- Hennebelle P., Chabrier G., 2011, *ApJ*, **743**, L29
- Hinshaw G., et al., 2013, *ApJS*, **208**, 19
- Hirano S., Hosokawa T., Yoshida N., Umeda H., Omukai K., Chiaki G., Yorke H. W., 2014, *ApJ*, **781**, 60
- Hollenbach D., McKee C. F., 1979, *ApJS*, **41**, 555
- Hopkins A. M., Beacom J. F., 2006, *ApJ*, **651**, 142
- Hosokawa T., Hirano S., Kuiper R., Yorke H. W., Omukai K., Yoshida N., 2015, preprint, ([arXiv:1510.01407](https://arxiv.org/abs/1510.01407))
- Inoue A. K., Shimizu I., Iwata I., Tanaka M., 2014, *MNRAS*, **442**, 1805

- Izotov Y. I., Orlitová I., Schaerer D., Thuan T. X., Verhamme A., Guseva N. G., Worseck G., 2016, *Nature*, **529**, 178
- Kashikawa N., et al., 2015, *ApJ*, **798**, 28
- Katz H., Ricotti M., 2013, *MNRAS*, **432**, 3250
- Katz H., Ricotti M., 2014, *MNRAS*, **444**, 2377
- Katz H., Kimm T., Sijacki D., Haehnelt M., 2016, preprint, ([arXiv:1612.01786](https://arxiv.org/abs/1612.01786))
- Kennicutt Jr. R. C., 1998, *ApJ*, **498**, 541
- Kim C.-G., Ostriker E. C., 2015, *ApJ*, **802**, 99
- Kim J.-h., Krumholz M. R., Wise J. H., Turk M. J., Goldbaum N. J., Abel T., 2013, *ApJ*, **775**, 109
- Kim Y., et al., 2015, *ApJ*, **813**, L35
- Kimm T., Cen R., 2014, *ApJ*, **788**, 121
- Kimm T., Cen R., Devriendt J., Dubois Y., Slyz A., 2015, *MNRAS*, **451**, 2900
- Kirk H., Myers P. C., 2011, *ApJ*, **727**, 64
- Kroupa P., 2001, *MNRAS*, **322**, 231
- Kroupa P., Weidner C., Pflamm-Altenburg J., Thies I., Dabringhausen J., Marks M., Maschberger T., 2013, The Stellar and Sub-Stellar Initial Mass Function of Simple and Composite Populations. p. 115, doi:10.1007/978-94-007-5612-0_4
- Krumholz M. R., McKee C. F., 2005, *ApJ*, **630**, 250
- Krumholz M. R., Stone J. M., Gardiner T. A., 2007, *ApJ*, **671**, 518
- Kuhlen M., Faucher-Giguère C.-A., 2012, *MNRAS*, **423**, 862
- Kulkarni G., Choudhury T. R., Puchwein E., Haehnelt M. G., 2016, preprint, ([arXiv:1607.03891](https://arxiv.org/abs/1607.03891))
- Lee H., Yoon S.-C., 2016, *ApJ*, **820**, 135
- Leethochawalit N., Jones T. A., Ellis R. S., Stark D. P., Zitrin A., 2016, preprint, ([arXiv:1606.05309](https://arxiv.org/abs/1606.05309))
- Leitet E., Bergvall N., Piskunov N., Andersson B.-G., 2011, *A&A*, **532**, A107
- Leitet E., Bergvall N., Hayes M., Linné S., Zackrisson E., 2013, *A&A*, **553**, A106
- Leitherer C., et al., 1999, *ApJS*, **123**, 3
- Leitherer C., Hernandez S., Lee J. C., Oey M. S., 2016, *ApJ*, **823**, 64
- Leonard P. J. T., Duncan M. J., 1988, *AJ*, **96**, 222
- Lopez L. A., Krumholz M. R., Bolatto A. D., Prochaska J. X., Ramirez-Ruiz E., Castro D., 2014, *ApJ*, **795**, 121
- Ma X., Kasen D., Hopkins P. F., Faucher-Giguère C.-A., Quataert E., Kereš D., Murray N., 2015, *MNRAS*, **453**, 960
- Ma X., Hopkins P. F., Kasen D., Quataert E., Faucher-Giguère C.-A., Kereš D., Murray N., Strom A., 2016, *MNRAS*, **459**, 3614
- Madau P., Fragos T., 2016, preprint, ([arXiv:1606.07887](https://arxiv.org/abs/1606.07887))
- Madau P., Haardt F., 2015, *ApJ*, **813**, L8
- Madau P., Haardt F., Rees M. J., 1999, *ApJ*, **514**, 648
- Madau P., Rees M. J., Volonteri M., Haardt F., Oh S. P., 2004, *ApJ*, **604**, 484
- Maio U., Petkova M., De Lucia G., Borgani S., 2016, *MNRAS*, **459**, 100
- Martizzi D., Faucher-Giguère C.-A., Quataert E., 2015, *MNRAS*, **450**, 504
- Matthee J., Sobral D., Santos S., Röttgering H., Darvish B., Mobasher B., 2015, *MNRAS*, **451**, 400
- McGreer I. D., Mesinger A., D’Odorico V., 2015, *MNRAS*, **447**, 499
- Meece G. R., Smith B. D., O’Shea B. W., 2014, *ApJ*, **783**, 75
- Mesinger A., Aykutalp A., Vanzella E., Pentericci L., Ferrara A., Dijkstra M., 2015, *MNRAS*, **446**, 566
- Mirabel I. F., Dijkstra M., Laurent P., Loeb A., Pritchard J. R., 2011, *A&A*, **528**, A149
- Mostardi R. E., Shapley A. E., Steidel C. C., Trainor R. F., Reddy N. A., Siana B., 2015, *ApJ*, **810**, 107
- Nomoto K., Tominaga N., Umeda H., Kobayashi C., Maeda K., 2006, *Nuclear Physics A*, **777**, 424
- Ocvirk P., et al., 2015, preprint, ([arXiv:1511.00011](https://arxiv.org/abs/1511.00011))
- Ono Y., et al., 2012, *ApJ*, **744**, 83
- Osterbrock D. E., Ferland G. J., 2006, Astrophysics of gaseous nebulae and active galactic nuclei
- Paardekooper J.-P., Khochfar S., Dalla Vecchia C., 2013, *MNRAS*, **429**, L94
- Paardekooper J.-P., Khochfar S., Dalla Vecchia C., 2015, *MNRAS*, **451**, 2544
- Padoan P., Nordlund Å., 2011, *ApJ*, **730**, 40
- Pawlik A. H., Schaye J., van Scherpenzeel E., 2009, *MNRAS*, **394**, 1812
- Pawlik A. H., Schaye J., Dalla Vecchia C., 2015, *MNRAS*, **451**, 1586
- Pentericci L., et al., 2014, *ApJ*, **793**, 113
- Planck Collaboration et al., 2014, *A&A*, **571**, A15
- Planck Collaboration et al., 2015, preprint, ([arXiv:1502.01589](https://arxiv.org/abs/1502.01589))
- Planck Collaboration et al., 2016, preprint, ([arXiv:1605.02985](https://arxiv.org/abs/1605.02985))
- Portegies Zwart S. F., 2000, *ApJ*, **544**, 437
- Razoumov A. O., Sommer-Larsen J., 2010, *ApJ*, **710**, 1239
- Reddy N. A., Steidel C. C., Pettini M., Bogosavljevic M., Shapley A., 2016, preprint, ([arXiv:1606.03452](https://arxiv.org/abs/1606.03452))
- Ricotti M., 2002, *MNRAS*, **336**, L33
- Ricotti M., Ostriker J. P., 2004, *MNRAS*, **352**, 547
- Ritter J. S., Safrank-Shrader C., Gnat O., Milosavljević M., Bromm V., 2012, *ApJ*, **761**, 56
- Robertson B. E., et al., 2013, *ApJ*, **768**, 71
- Rosdahl J., Teyssier R., 2015, *MNRAS*, **449**, 4380
- Rosdahl J., Blaizot J., Aubert D., Stranex T., Teyssier R., 2013, *MNRAS*, **436**, 2188
- Rutkowski M. J., et al., 2016, *ApJ*, **819**, 81
- Sana H., et al., 2012, *Science*, **337**, 444
- Schaerer D., 2002, *A&A*, **382**, 28
- Schenker M. A., Ellis R. S., Konidaris N. P., Stark D. P., 2014, *ApJ*, **795**, 20
- Schmidt M., 1959, *ApJ*, **129**, 243
- Semenov D., Henning T., Helling C., Ilgner M., Sedlmayr E., 2003, *A&A*, **410**, 611
- Shapiro P. R., Giroux M. L., 1987, *ApJ*, **321**, L107
- Shapley A. E., Steidel C. C., Strom A. L., Bogosavljević M., Reddy N. A., Siana B., Mostardi R. E., Rudie G. C., 2016, preprint, ([arXiv:1606.00443](https://arxiv.org/abs/1606.00443))
- Sheth R. K., Tormen G., 2002, *MNRAS*, **329**, 61
- Shull J. M., Harness A., Trenti M., Smith B. D., 2012, *ApJ*, **747**, 100
- Siana B., et al., 2007, *ApJ*, **668**, 62
- Siana B., et al., 2010, *ApJ*, **723**, 241
- Siana B., et al., 2015, *ApJ*, **804**, 17
- Smith B. D., Hallman E. J., Shull J. M., O’Shea B. W., 2011, *ApJ*, **731**, 6
- Smith B. D., Wise J. H., O’Shea B. W., Norman M. L., Khochfar S., 2015, *MNRAS*, **452**, 2822
- So G. C., Norman M. L., Reynolds D. R., Wise J. H., 2014, *ApJ*, **789**, 149
- Speagle J. S., Steinhardt C. L., Capak P. L., Silverman J. D., 2014, *ApJS*, **214**, 15
- Stanway E. R., Eldridge J. J., Becker G. D., 2016, *MNRAS*, **456**, 485
- Steidel C. C., Pettini M., Adelberger K. L., 2001, *ApJ*, **546**, 665
- Teyssier R., 2002, *A&A*, **385**, 337
- Thornton K., Gaudlitz M., Janka H.-T., Steinmetz M., 1998, *ApJ*, **500**, 95
- Tilvi V., et al., 2014, *ApJ*, **794**, 5
- Topping M. W., Shull J. M., 2015, *ApJ*, **800**, 97
- Toro E. F., Spruce M., Speares W., 1994, *Shock Waves*, **4**, 25
- Turk M. J., Abel T., O’Shea B., 2009, *Science*, **325**, 601
- Turk M. J., Oishi J. S., Abel T., Bryan G. L., 2012, *ApJ*, **745**, 154
- Tweed D., Devriendt J., Blaizot J., Colombi S., Slyz A., 2009, *A&A*, **506**, 647
- Vanzella E., et al., 2010, *ApJ*, **725**, 1011
- Visbal E., Haiman Z., Bryan G. L., 2015, *MNRAS*, **453**, 4456
- Walch S. K., Whitworth A. P., Bisbas T., Wünsch R., Hubber D., 2012, *MNRAS*, **427**, 625
- Weidner C., Kroupa P., Bonnell I. A. D., 2010, *MNRAS*, **401**, 275
- Weingartner J. C., Draine B. T., 2001, *ApJ*, **548**, 296
- Whalen D., Abel T., Norman M. L., 2004, *ApJ*, **610**, 14
- Wise J. H., Cen R., 2009, *ApJ*, **693**, 984
- Wise J. H., Abel T., Turk M. J., Norman M. L., Smith B. D., 2012a, *MNRAS*, **427**, 311
- Wise J. H., Turk M. J., Norman M. L., Abel T., 2012b, *ApJ*, **745**, 50
- Wise J. H., Demchenko V. G., Halicek M. T., Norman M. L., Turk M. J., Abel T., Smith B. D., 2014, *MNRAS*, **442**, 2560

- Wolfire M. G., McKee C. F., Hollenbach D., Tielens A. G. G. M., 2003, [ApJ](#), **587**, 278
- Woo J., Courteau S., Dekel A., 2008, [MNRAS](#), **390**, 1453
- Woosley S. E., Weaver T. A., 1995, [ApJS](#), **101**, 181
- Xu H., Wise J. H., Norman M. L., Ahn K., O'Shea B. W., 2016, preprint, ([arXiv:1604.07842](#))
- Yajima H., Choi J.-H., Nagamine K., 2011, [MNRAS](#), **412**, 411
- Yoshida N., Omukai K., Hernquist L., Abel T., 2006, [ApJ](#), **652**, 6